Propagation Characteristics of Plasmonic Gap Waveguiding Structures

Undergraduate Honors Thesis by

Galen Brandt Hoffman

In Partial Fulfillment of the Requirements for

Graduation with Distinction

The Ohio State University
Department of Electrical and Computer Engineering

Columbus, Ohio

2007

(Defended May 11th 2007)

Acknowledgements

I would like to thank a couple of people who aided in the completion of this project.

First and foremost, I would like to thank my research advisor, Professor Ronald Reano. The thing that I most appreciate about his management style is his optimism and goal-oriented attitude. These are important traits to have in the field of integrated optics, which is extremely challenging and full of unforeseen developments. Additionally, he has been proactive in making sure that I have the tools I needed to complete the project. Another aspect of his management style that has been beneficial to this work is his “open door” policy. I have always been able to go to his office and discuss pressing problems. This has kept the channel of communication between us free-flowing and has resulted in pointed and productive meetings.

I would like to thank Professor Fernando Teixeira for taking time out of his no doubt busy schedule to be the second professor in my oral defense of this project and to lend his expertise in critical analysis of my work. Professor Teixeira and one of his graduate students, Kyung Young Jung, have also contributed to this work by meeting with our group and sharing their work, insights and articles on the current state of the art in plasmonic waveguiding.

Abstract

As devices in current microprocessors continue to scale to ever decreasing dimensions, the concurrent increase in the RC time constants drive the need for next generation interconnects that can propagate signals at higher speeds. Plasmonic waveguides, using materials with a negative permittivity such as the noble metals, have the ability to propagate light signals over the length scale required for microprocessors while keeping the spot size of the light below the diffraction limit. Light propagating in a plasmonic waveguide has the advantage over electrons in a metal wire because it can propagate signals about three orders of magnitude faster. The price that is paid for confining light to dimensions on the order of tens of nanometers is a finite propagation length, due to the finite conductivity of the negative index material.

A class of plasmonic waveguides is examined in this research. These waveguides consist of a dielectric core bounded on either side by metallic walls, and are known as "plasmonic gap waveguides." Physically realizable structures consist of metal films with rectangular channels or gaps etched through them. It is found that making the gap smaller, increasing the refractive index of the dielectric material in the gap above about 1.5, and increasing the frequency of the excitation field has the effect of decreasing the propagation length. Propagation lengths on the order of 100 micrometers or less can be obtained with this type of waveguiding structure. This makes it useful for medium and short distance interconnects. Making the height to width aspect ratio of the gap large enough will allow for more vertical modes to propagate. The fundamental mode is of primary interest because it displays the lowest loss, is the easiest to excite, and is the highest confined mode for subwavelength geometries. As expected, there is transverse power flow into the metal, where it is dissipated. The power flow in the direction of propagation is strongest at the four metal corners of the waveguide. The high power focusing ability of this waveguide could be harnessed to exploit optical nonlinearities of materials used in the core, which could lead to the development of an all-optical plasmonic switch.

Table of Contents

List of Figures

Chapter 1: Introduction

1.1 Motivation for This Work

As human society continues to develop, it becomes more reliant on advanced technology to make processes more efficient, faster, and less expensive. One area that has made huge progress in the past few decades, and continues to do so today, is computing. The first microprocessor produced by Intel in 1971, called the "4004", was composed of about 2300 transistors and implemented a 4 bit instruction miroarchitecture [1]. In 2006, Intel released the dual core "Conroe" processor, which had more than 100,000 times the number of transistors, and is capable of executing 64 bit instructions at 2.93 GHz [2]. This improvement in performance is in accordance with the well-known Moore's Law, a trend that was predicted by Intel co-founder Gordon Moore in 1965 that says the number of transistors in microprocessors will double every 24 months [3]. This increase in the number of transistors translates into more performance by increasing the number of switching elements able to process information, as well as their switching speed, and is accomplished by a decrease in the transistor size, which is usually given by a nominal minimum channel (in reference to the length of a channel in a metal oxide semiconductor, or MOS transistor) length, also known as the "feature size" of a microelectronic circuit. Later this year, Intel plans to release the code-named "Penryn" processors that have feature sizes of 45 nm [4]. While transistors may benefit from this shrinking however, the electrical interconnects that stitch them together have an increased effective RC time constant that increases the time required for them to charge and discharge, and they are becoming the limiting factor in the speed of information processing [5,6]. There has thus been a large push in recent years to develop other means of transmitting information on a scale on the order of 1 cm (roughly the current size of a microprocessor chip).

One proposed method is to use light pulses as signals rather than electrons. Research is being done on many fronts to develop practical optical interconnects and devices, from nonlinear all-optical switching methods [7,8], to ring resonator filtering schemes [9], and also on the techniques needed to fabricate such devices [10,11]. Typically, dielectric optical waveguides are used to confine light using the principle of total internal reflection, in the same manner as the optical fibers used for long distance communications, and are fabricated on a planar process as rectangular, rather than cylindrical, structures [12]. A major advantage of using light as a carrier of information is its speed (on the order of 10^8 meters per second), which is about three orders of magnitude faster than the saturation velocity of electrons conducting in a semiconductor (~10^5 meters per second in silicon [13]). On the other hand, photons are not as localized as electrons and require much larger waveguides in order to achieve proper confinement. The uncertainty principle limits light confinement to [14]

$$a_{min} = \frac{\lambda_0}{2*n} \tag{1.1.1}$$

Here a_{min} is the minimum mode width, λ_0 is the free space wavelength, and n is the refractive index of the dielectric medium in which the light is propagating. This minimum boundary on the spot size limits how small a *dielectric* optical waveguide can be if it is to effectively confine the propagating light. For a wavelength of 1.55 µm and a core index of 1.5, the minimum dielectric mode width is about 0.517 µm. Electrical interconnects in current microprocessors are about one fifth of this or less [15]. The natural goal is to find a way to defeat this limit, so as to propagate signals at the speed of light while being confined below the minimum diffraction spot size.

Over 60 years ago, Ugo Fano published a work describing the interaction of light impinging on a corrugated metallic grating [16]. In this work, he described how light, polarized such that the magnetic field is tangential to a metal-dielectric interface, can set up a wave guided along the surface after it is scattered by the grating. This surface mode is strongly coupled to electron oscillations in the metal and is attenuated in the direction of propagation due to the ohmic loss of the electron motion. Later, Eleftherios Economou theoretically investigated such modes propagating in metal-dielectric-metal and dielectric-metal-dielectric layered structures [17]. Theoretical work on such modes was also done by Kaminow, who demonstrated that a propagating mode can exist in a metal-dielectric-metal sandwich structure below the diffraction limit. He was also able to demonstrate a clear tradeoff between confinement and the finite propagation length [18]. Eventually, these quantized surface charge density oscillations were called surface plasmon polaritons (SPPs) and the area of photonics dealing with manipulating such waves was called "plasmonics [19]." Much theoretical and experimental work has been done on different waveguiding methods. The advent of such processing technologies as electron beam lithography and nanoimprint lithography in the past few years has aided in the fabrication of these nanometer scale metallic structures. The three dimensional, realizable, structures that have been studied fall into three broad categories: arrays of metallic nanoparticles with various geometries, channels or grooves in metallic films, and thin metal strips of finite width. Each of these classes of waveguides presents a different way of exchanging higher confinement for smaller propagation lengths. The nanoparticles tend to have propagating modes with dimensions on the order of 50-100 nm, but the propagation lengths do not go much beyond a few hundred nanometers [20]. The channel or groove waveguides can confine the light to within around 100-200 nm while maintaining propagation lengths in the tens of microns [21]. Finally, the thin metal strip waveguides support the so-called long range surface plasmon polariton modes (LRSPPs) which have been shown to propagate over lengths on the order of millimeters to centimeters [22]. However, these metal strips do not provide high confinement, as the evanescent tails of the modes have an extinction length of around 3-4 microns for the LRSPPs [23]. See Figure 1.1 below for a graphical depiction of one component of the mode fields of such waveguides. One can see that the nanoparticle chain has the lowest propagation length. Both the nanoparticle chain (Figure 1.1a) and the metal strip (Figure 1.1c) have evanescent tails that extend into the surrounding medium and are not highly localized within the waveguide, making these waveguides more useful for applications where they could be used to sense refractive index changes in the surrounding material. The radiation is very well confined to the metal gap (Figure 1.1b), however, and this makes it much better suited for signaling interconnect applications, because many such waveguides could be placed in close proximity horizontally without experiencing cross talk. These field distributions were obtained using a 2-dimensional commercial finite difference time domain (FDTD) code called *FullWave*™ developed by the company *RSoft*™.

Given that it was my goal to explore plasmonic waveguiding for the purposes of optical interconnects, I decided to explore waveguides of the second type: plasmon waves propagating in metal gap structures.

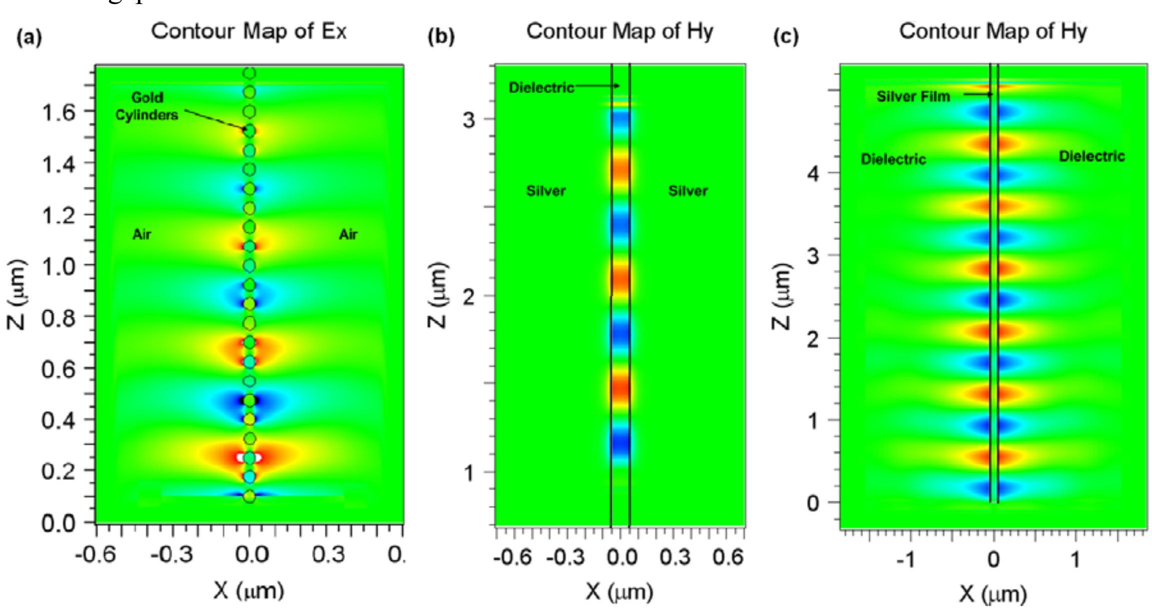

Figure 1.1: Depiction of the mode field distributions for two-dimensional waveguides excited with TM polarized radiation. (a) A chain of gold cylinders of radius 50 nm and spacing 75 nm in air excited at 0.454 μm wavelength (transverse mode), (b) a dielectric (index of 2) gap 100 nm wide in a silver film excited at 1.55 μm wavelength, (c) a metal film 100 nm wide embedded in a dielectric of index 2 excited at 1.55 μm wavelength. This was simulated using 2-dimensional FDTD code developed by *RSoft*™.

These currently show the most promise and provide the best, middle-of-the-road tradeoff between loss and confinement. Though the modes of this waveguide can be analytically determined, given that it is an ideal 2-dimensional waveguide that is infinite in the direction normal to the plane of this page, it is not physically realizable. The physically realizable analog to this waveguide is shown below in Figure 1.2. This consists of a dielectric core of width *w* etched into a metal film of height *h*. The film is deposited on a substrate and is protected by a cover material. In general, the cover, core, and substrate will have different refractive indices. The coordinate system is as shown, with the waveguide structure being infinite in the propagation direction, which is the *Z* direction. As was discussed briefly above, the light propagating in this structure must be polarized such that the primary magnetic field component is along the metal-dielectric interfaces of the core to obtain a plasmon wave, which is in the *Y* direction in this case. A special attribute of this simple waveguiding structure is that the propagating light is confined horizontally by the metal walls, but it not as tightly confined vertically. This leads to a logical question: what sort of cross-talk can occur between two such waveguides when one is placed above the other?

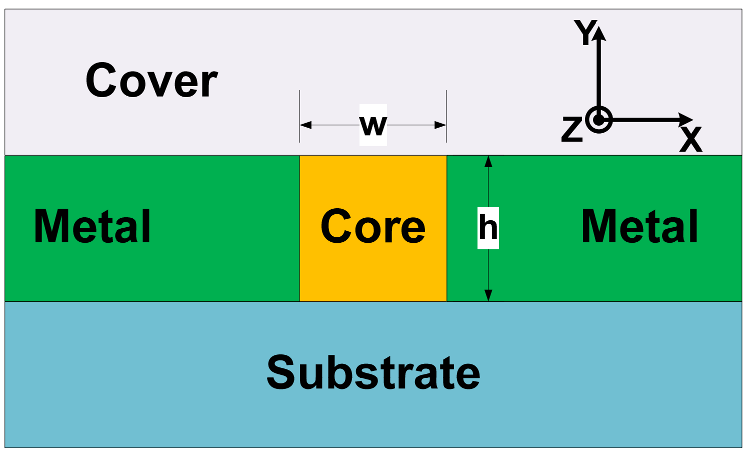

Figure 1.2: Schematic diagram of the physically realizable plasmonic gap waveguide.

A similar analysis has already been done for waveguides of the metal strip type [25], but again, those waveguides do not provide subwavelength confinement, and exhibit coupling lengths over *hundreds* of microns, and so this type of coupling cannot lead to compact, highly integrated devices. This coupled-gap structure could be altered, using nonlinear optical materials, to function as an all optical switch [26]. This will be left as the topic for a future exploration, however. The purpose of this investigation is to determine the propagation characteristics of electromagnetic radiation in the plasmonic gap waveguide.

1.2 Outline of this Thesis

This report will explore the propagation characteristics of optical and near-infrared electromagnetic radiation in plasmonic waveguiding structures. Chapter two will present a simple model for approximating the frequency-dependent relative permittivity of metals, known as the Drude model. The next chapter will give an analytical treatment of the single metal-dielectric interface, solving for the propagation constants and the field distribution. Chapter four will cover the metal-insulator-metal waveguide, focusing on the tradeoff between loss and mode confinement. Chapter five gives a numerical analysis of the field distributions and propagation constants for the finite height plasmonic gap waveguide.

Chapter 2: Modeling the Frequency-Dependent Relative Permittivity of Metals

2.1 The Drude Model

As was mentioned above, a plasmon wave is a light wave coupled to charge density oscillations on the surface of a highly conductive metal, like gold. In such metals, there is a significant density of free carriers such that the metal can be though of as an electron gas or "cold plasma [27]." Because the oscillation and damping characteristics of the electrons change with the excitation energy, it is therefore necessary model the frequency response of the electrons in order to properly capture their effect on the wave's propagation. The macroscopic complex relative electric permittivity of the metal accounts for these effects, and can be derived as a function of frequency using the application of *classical* electromechanical principles [28]:

$$\varepsilon(\omega) \quad = \quad \varepsilon(\mathrm{inf}) \quad - \quad \frac{\omega_p^2}{\omega^2 \quad - \quad i^*\Gamma^*\omega} \tag{2.1.1}$$

Here $\varepsilon(\omega)$ is the complex relative permittivity of the metal, $\varepsilon(inf)$ is the permittivity of the metal at the limit of infinite frequency, ω_p is the bulk radial plasma frequency, which represents the natural frequency of the oscillations of free conduction electrons, Γ is the radial damping frequency due to electron scattering events, and ω is the radial frequency of the incident electromagnetic radiation. The plasma frequency ω_p can itself be expressed in terms of basic material parameters:

$$\omega_p \quad = \quad \sqrt{\frac{ne^2}{m^*\varepsilon_0}} \tag{2.1.2}$$

Here, n is the free carrier concentration, m^* is the effective electron mass, e is the fundamental unit of electric charge, and ε_0 is the free space permittivity [27].

Usually the complex conjugate of Equation 2.1.1 is cited in the literature as the Drude model [23,29]. This violates physical reasoning, however. If one rearranges Equation 2.1.1 one arrives at the resulting equation:

$$\varepsilon(\omega) \quad = \quad \left(\varepsilon(\mathrm{inf}) \quad - \quad \frac{\omega_p^2}{\omega^2 + \Gamma}\right) \quad - \quad i\cdot\frac{\omega_p^2\Gamma}{\omega\left(\omega^2 + \Gamma^2\right)} \tag{2.1.3}$$

Clearly, all of the parameters in the equation above are real and positive, and so the imaginary part of the permittivity is negative. This is consistent with Ampere's Law, when one takes the current density as being driven by the electric field of the radiation:

$$\nabla \times \vec{H} \quad = \quad \vec{J} + i\omega\varepsilon_r\varepsilon_0\,\vec{E} \tag{2.1.4}$$

Substituting in ($\vec{J} = \sigma\vec{E}$) and factoring ($i\omega\varepsilon_0$):

$$\nabla \times \vec{H} = i\omega\omega_0\left(\varepsilon_r - i\frac{\sigma}{\varepsilon_0\omega}\right)\vec{E} \qquad (2.1.5)$$

Here, ε_r is the real part of the permittivity, and σ is the conductivity. Because of the way that the current density is being treated in Equation 2.1.5, which will be carried through for the rest of the analysis, any currents that do exist really manifest themselves as *displacement currents*, and so are in general out of phase with the curl of the magnetic field. The net complex permittivity due to the finite conductivity:

$$\varepsilon(\omega) = \left(\varepsilon_r - i\frac{\sigma}{\varepsilon_0\omega}\right) \qquad (2.1.6)$$

And matching terms with Equation 2.1.3:

$$\varepsilon_r(\omega) = \left(\varepsilon(\mathrm{inf}) - \frac{\omega_p^2}{\omega^2 + \Gamma}\right) \qquad (2.1.7)$$

$$\sigma(\omega) = \frac{\varepsilon_0\,\omega_p^2\Gamma}{\left(\omega^2 + \Gamma^2\right)} \qquad (2.1.8)$$

If the more widely stated version of the Drude model (the complex conjugate of Equation 2.1.1) was used here, it would have required the conductivity to be negative, which is unphysical, at least for passive media without gain. There are other physical reasons why the negative conjugate Drude model should be used, and this will be discussed in Chapter 3.

2.1 Comparison of the Drude Model with Experimental Data and Its Predictive Limitations

One could take the effort to calculate the three input parameters of Equation 2.1.1 from first principles using Equation 2.1.2, but usually they are used as curve-fitting parameters to match the model with experimental data [29]. Because this theory is classical, it does not take into higher energy quantum effects such as the energy band structure of the metal that leads interband transitions that affect (increase) the absorption of the light (the loss). Johnson and Christy (JC) experimentally demonstrated the limitation of the Drude model by showing how *ε(ω)* rapidly diverges from the predicted value as the energy of the exciting photons increased above some value [24]. Nordlander and Oubre (NO) fit the Drude model to JC's experimental data and found that major divergence between predicted and experimental results occurs below a wavelength of 400 nm for Ag [29]. Below in Figure 2.1 is presented the same sort of divergence analysis for Au. One can see that a large divergence between theory and experiment occurs above about 1.7

eV or below 730 nm free space wavelength. More complex models of the dielectric constants of metals at higher energies are available, but the Drude model provides a good first-order approximation as long as the wavelength is restricted properly. The NO Drude parameters for Ag are $\varepsilon(inf)$ = 5.0, Γ = 0.0987 eV, and ω_p = 9.5 eV. The corresponding parameters for Au are 9.5, 0.06909 eV, and 8.9488 eV, respectively.

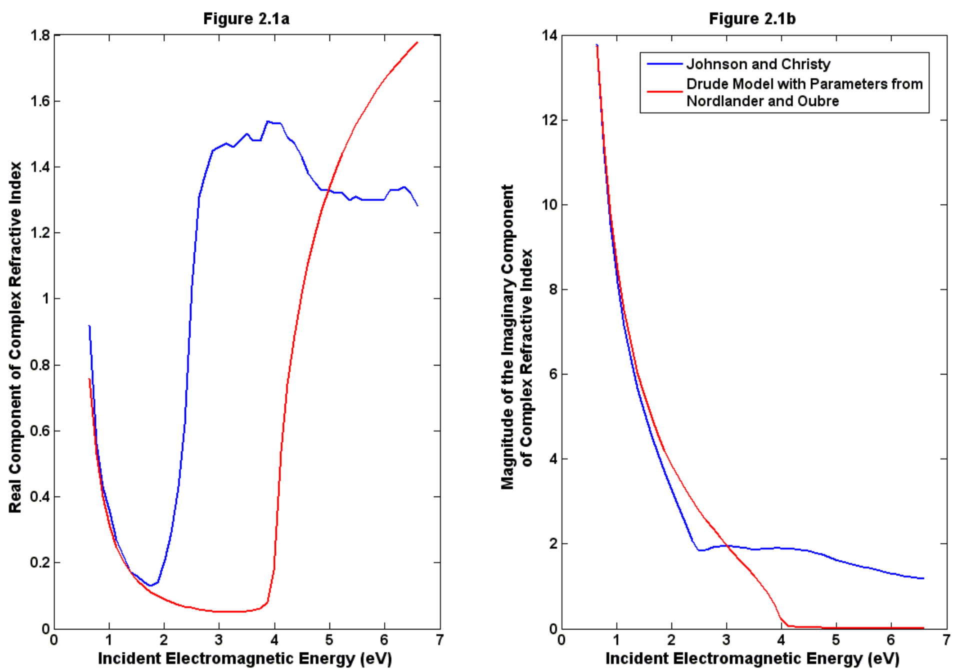

Figure 2.1: The (a) real and (b) imaginary components of the complex refractive index for Au versus incident electromagnetic energy for the Drude model with parameters from Nordlander and Oubre (red line) and experimentally determined by Johnson and Christy (blue line).

Using the parameters for Au, at a telecom wavelength of 1.55 μm, $\varepsilon(\omega)$ = -114.4 - i*10.69. It is the negative real part of $\varepsilon(\omega)$ that allows the surface plasmon wave to exist, and the imaginary part that leads to the finite propagation length, and is representative of the ohmic loss within the metal due to its finite conductivity. Both the Drude model, with the parameters from NO and experimental data available in the Handbook of Optical Constants of Solids (HOCS) are used in the analyses of this thesis [30].

Chapter 3: Light Confinement at a Single Interface

3.1 Analytical Setup

This section will show how electromagnetic radiation can be guided at a single metal-dielectric interface. This is actually a special case of the well-known reflection-refraction of an infinite plane wave at a single interface between two semi-infinite media problem. A diagram of the setup for the transverse magnetic (TM) polarization is shown below in Figure 3.1 [31]. This consists of an incident plane wave in Region 1 (with a permittivity of ε_1) specified by H_i and E_i impinging on the surface at an angle of incidence θ_i along with corresponding reflected and transmitted waves (whose components are denoted with the respective r and t subscripts). The wave vectors, denoted by k's, are also shown. These vectors are completely in-plane and have components:

$$\vec{k}_i = \hat{x}\cdot k_{ix} + \hat{z}\cdot k_{iz} \tag{3.1.1a}$$

$$\vec{k}_r = \hat{x}\cdot k_{rx} + \hat{z}\cdot k_{rz} \tag{3.1.1b}$$

$$\vec{k}_t = \hat{x}\cdot k_{tx} + \hat{z}\cdot k_{tz} \tag{3.1.1c}$$

The functional forms of the magnetic fields of the three plane waves are given below:

$$\vec{H}_i = \hat{y}\cdot H_{i0} e^{-j\cdot(k_{ix}\cdot x + k_{iz}\cdot z - \omega\cdot t)} \tag{3.1.2a}$$

$$\vec{H}_r = \hat{y}\cdot H_{r0} e^{-j\cdot(k_{rx}\cdot x + k_{rz}\cdot z - \omega\cdot t)} \tag{3.1.2b}$$

$$\vec{H}_t = \hat{y}\cdot H_{t0} e^{-j\cdot(k_{tx}\cdot x + k_{tz}\cdot z - \omega\cdot t)} \tag{3.1.2c}$$

These give the functional form of the magnetic field at all points in space and time. When the components of the wavevector are real, the wave oscillates only, but when they become complex, they also have a component of exponential decay. Using the following relationship, one can solve for the electric field components:

$$\vec{E} = -\eta\cdot\hat{k}\times\vec{H} \tag{3.1.3}$$

Here, η is the intrinsic impedance of the region in question, and $\hat{k}$ is the unit vector corresponding to the wave vector of the respective plane wave. Since the magnitude of the electric field is merely a scalar multiple of the magnetic field, it has the same dependence as a function of displacement.

In order to understand what is happening at the interface, it is instructive to examine the Fresnel reflection coefficients for both polarizations (TM and transverse electric (TE)), assuming that the materials on either side of the interface are nonmagnetic (the relative magnetic permeability = 1) [31]:

$$\Gamma_{TE} = \frac{|E_{rTE}|}{|E_{iTE}|} = \frac{n_1 * \cos(\theta_i) - n_2 * \cos(\theta_t)}{n_1 * \cos(\theta_i) + n_2 * \cos(\theta_t)} \tag{3.1.4}$$

$$\Gamma_{TM} = \frac{|E_{rTM}|}{|E_{iTM}|} = \frac{n_2 * \cos(\theta_i) - n_1 * \cos(\theta_t)}{n_2 * \cos(\theta_i) + n_1 * \cos(\theta_t)} \tag{3.1.5}$$

Here, Γ_* represents the ratio of the incident to reflected magnitudes of the electric field for the respective polarization, n_1 and n_2 are the indices of refraction for the first and second materials, respectively, θ_i is the angle of incidence, and θ_t is the angle of transmission. In order to look for a surface mode, one would like to have no radiation away from the interface, so this corresponds to setting the reflection coefficients to zero. If one does this for equations 3.1.4 and 3.1.5, and substitutes in Snell's Law, one can show that for the TE case [32],

$$n_1 = n_2 \tag{3.1.6}$$

Clearly, for nonmagnetic materials, setting the reflection coefficient to zero in the TE case requires that the interface not exist. For the TM case one obtains [33]:

$$k_z = k_0 * \sqrt{\left(\frac{\varepsilon_1 * \varepsilon_2}{\varepsilon_1 + \varepsilon_2}\right)} \tag{3.1.7}$$

Here, k_z is the propagation constant in the direction of propagation, k_0 is the free space propagation constant, ε_1 is the relative permittivity of medium 1, and ε_2 is the relative

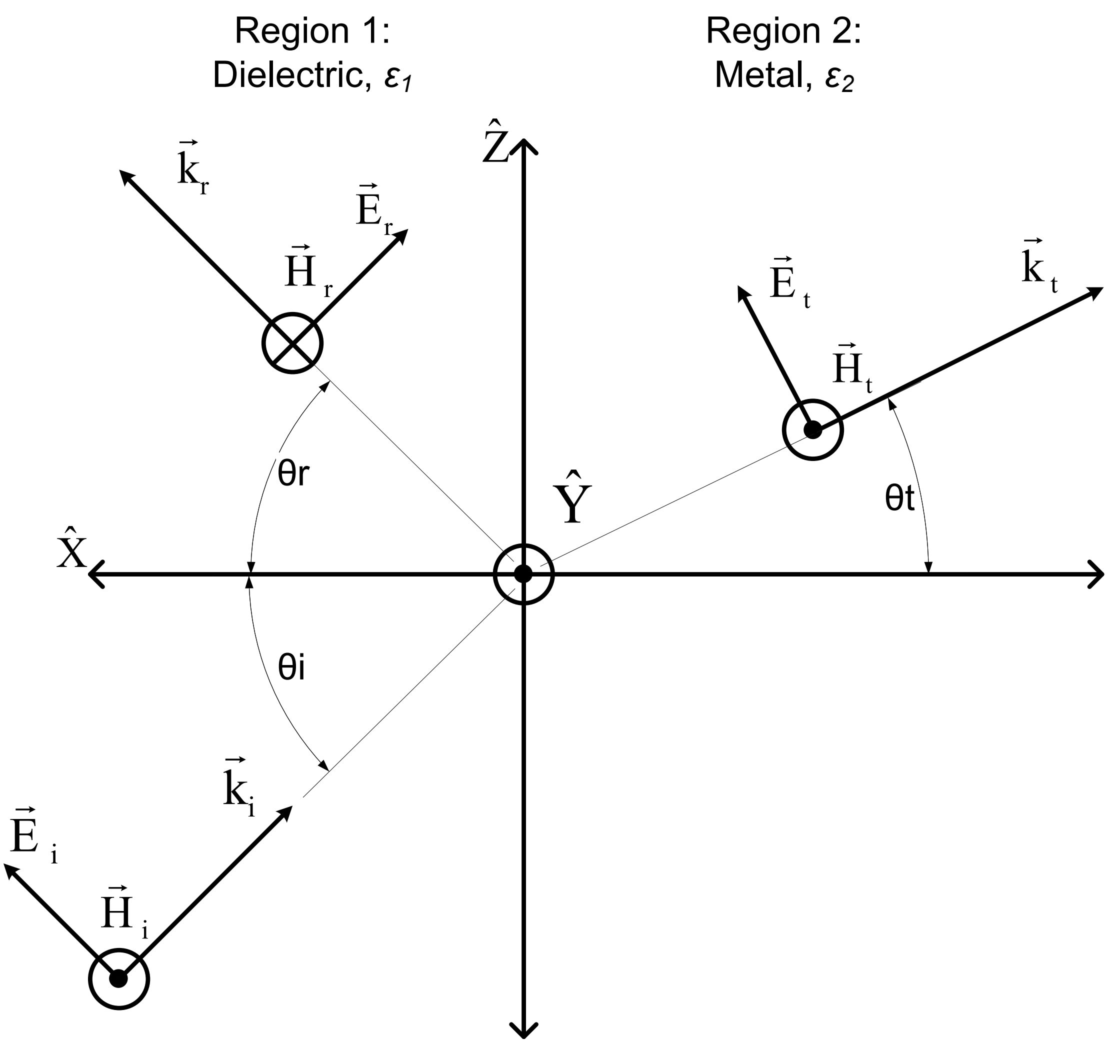

Figure 3.1: Standard setup for determining the reflection and refraction of an incident plane wave at the interface between two semi-infinite media.

permittivity of medium 2. The propagation constant is the same in the *Z* direction in both regions because of the tangential phase matching condition at the interface that is expressed by Snell's Law. So clearly it is only with a component of the incident light polarized such that the magnetic field is tangential to the interface that can one set up a surface wave using nonmagnetic materials. Also, one can easily use the Pythagorean Theorem to find the transverse propagation constants k_{z1} and k_{z2} are given below:

$$k_{x1} = k_0 * \left(\frac{\varepsilon_1}{\sqrt{\varepsilon_1 + \varepsilon_2}} \right) \tag{3.1.8}$$

$$k_{x2} = k_0 * \left(\frac{\varepsilon_2}{\sqrt{\varepsilon_1 + \varepsilon_2}} \right) \tag{3.1.9}$$

The wave described by Fano decayed evanescently away from the interface on both sides, which implies that k_{x1} and k_{x2} should be imaginary. Also, this wave propagates along the interface, which implies that k_z should be real. These conditions are satisfied only in the case when $|\mathrm{Re}\{\varepsilon_2\}| > \mathrm{Re}\{\varepsilon_1\}$,$\mathrm{Re}\{\varepsilon_2\} < 0$, and $\mathrm{Re}\{\varepsilon_1\} > 0$. As was discussed above, an interface between an insulator and a noble metal such as Au is able to satisfy this requirement at telecom and optical frequencies. Thus, an interface between a dielectric and a noble metal such as Au is able to support the so-called surface plasmon wave. However, because $\varepsilon(\omega)$ is going to be complex due to the damping of electron motion in the metal, the wave will decay exponentially in the direction of propagation.

3.2: The Single Interface Field Solution

It will now be helpful to go through an example showing the resulting components of the fields, the wave vector, as well as time average power flow. For this setup, the metal will be silica in Region 1, and silver in Region 2, as depicted above in Figure 3.1. In the optical and near infrared spectrum (say from 400 to 2,000 nm free space wavelength (λ_0)), which is of interest for biosensing and telecommunications applications, the real part of the silver's permittivity, ε_m is negative and has a magnitude much larger than that of the imaginary part. At λ_0 = 1μm, using HOCS's experimental data, ε_m = -45.6 – i2.90. In order to find the wave vector components in both regions, Equations 3.1.7 - 3.1.9 will be used. It will also be assumed that the Ag was deposited on silica, which has a relative permittivity, ε_d of about 1.45 at this wavelength [34]. For k_z, Equation 3.1.7 yields (7.69e6 – i7.98e3) radians per meter, taking the fourth quadrant root. Substituting this value into Equations 3.1.2, one can see that this leads to propagation in the positive Z direction with exponential decay. Taking the negative root would have led to a wave travelling and decaying in the opposite direction. The length over which the amplitude of the field dies down to 1/e of its initial value is 1/(7.98e3) = 0.125 mm. For the transverse wave vector k_x in the metal, Equation 3.1.9 yields (-1.32e6+i4.3e7) rad/m, taking the second quadrant root. This leads to propagation in the negative X direction, away from the interface. The field also decays into the metal, because with the chosen coordinate system, the x values are negative with increasing magnitude. Here, the "skin depth" or 1/e field decay length is given by 1/(4.3e7) = 23.3 nm, which is typical of noble metals at these frequencies [23]. Finally, for the transverse wave vector in the dielectric, Equation 3.1.8 yields –(4.48e4+i1.37e6) rad/m, taking the third quadrant root. This corresponds to evanescent decay away from the interface into the dielectric, and oscillation towards the interface. The skin depth here is 730 nm. Clearly the wave decays much faster in the metal. Also, the wave fronts are tilted towards the interface, indicating power flow into the metal. The real component of the transverse wave vector is also larger in the metal, indicating that the wave travels faster, in the transverse direction, in the dielectric. Figure 3.2 below gives a qualitative (i.e. not to scale) diagram showing triangles representing the real parts of the wave vector components in each region.

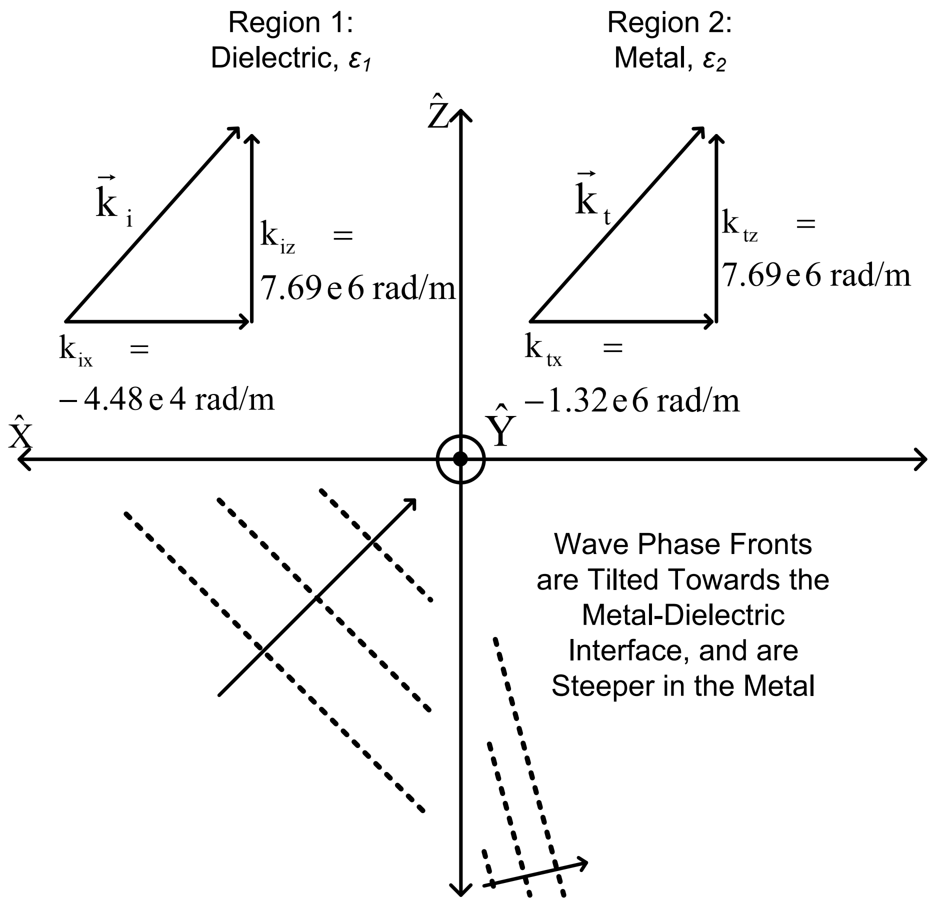

Figure 3.2: Orientation of the real components of the wave vectors of the single interface surface plasmon wave for the case where the metal is Ag, the dielectric is silica, and the free space wavelength is 1 μm. The phase fronts of the wave in both regions are also shown.

It is important to note here that if the other, conjugate version of the Drude model had been chosen, all of the propagation constants would also be conjugated, and this would have resulted in exponential grown in the direction of propagation. Shown below in Figure 3.3 is an arrow plot of the resulting electric fields overlaid on a color plot of the magnetic fields for this example. The amplitude of the magnetic field is taken as 1 here. One can see that the field decay is much more rapid in the metal, as was noted before. The actual tilt of the wave fronts is very slight compared to the rate of decay away from the interface. The electric field alternates between bending toward and away from the interface. At the locations where it is pointing purely in a transverse direction, it shows a divergence due to a necessary sign change across the interface. This indicates that there is an instantaneous charge density wave at the interface travelling along with the electromagnetic radiation, as one would expect.

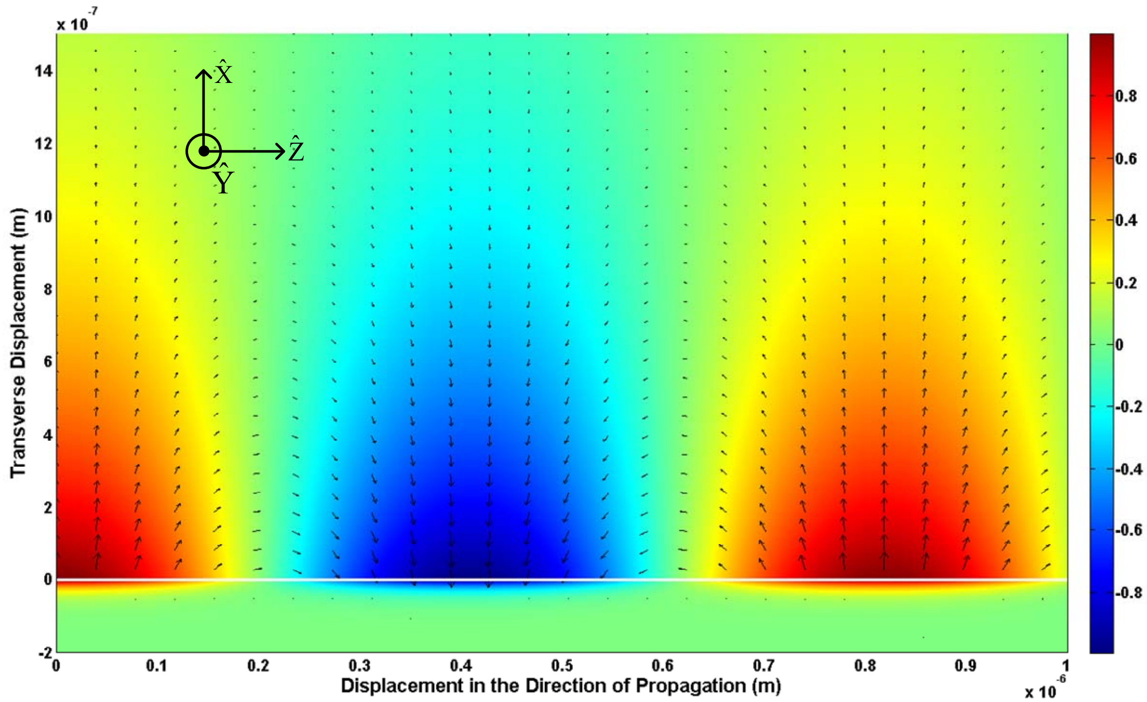

Figure 3.3: Color plot (analytical solution using *MATLAB*™) of the magnetic field and arrow plot of the electric field as a function of transverse and propagation direction displacement for a plasmon wave (TM polarization) at an infinite Ag-SiO_2 interface. The white line denotes the interface.

This is difficult to see with the electric field being so weak in the metal, but is caused by the requirement that the normal component of the electric flux density, D_x, needing to be continuous across the interface due to the assumption in the derivation of the functional form of the fields that the *static* volume and surface charge densities be zero. Because the permittivity changes sign across the interface, the normal component of the electric field is phase shifted by the negative of the metal's permittivity's phase, which here almost 180˚.

The transverse power flow of this wave is towards and into the metal. This can be readily seen. For this simple 2-dimensional case, only three field components are present: H_y, E_x, and E_z. The power flow is defined by the time-averaged Poynting vector:

$$\vec{S}_{avg} = \frac{1}{2}\mathrm{Re}\left(\vec{E}\times\vec{H}^*\right) \quad (3.2.1)$$

Substituting in the non-zero field components:

$$\vec{S}_{avg} = \frac{1}{2}\mathrm{Re}\left\{\left(\hat{x}\cdot E_{ox} + \hat{z}\cdot E_{oz}\right)\times\left(\hat{y}\cdot H_{oy}{}^*\right)\right\} \quad (3.2.2)$$

Performing the cross-product and separating out the *x* and *z* components:

$$\vec{S}_{avg} = -\hat{x}\cdot\frac{1}{2}\mathrm{Re}\left\{E_{oz}\cdot H_{oy}^{*}\right\} + \hat{z}\cdot\frac{1}{2}\mathrm{Re}\left\{E_{ox}\cdot H_{oy}^{*}\right\} \tag{3.2.3}$$

Here, E_{ox}, E_{oz}, and H_{oy} are the respective complex field magnitudes. Taking the field distribution determined in the example above (using the equations in Section 3.1 of this chapter), the *z* and *x* components of the time average Poynting vector are plotted in Figures 3.4 and 3.5, respectively. When one examines the *z* power flow, one can see that it is much larger in the dielectric than in the metal. The most interesting thing about this though is that in the metal, the time average power flows in the direction opposite that of the wave's propagation, as shown by the slight dip into the negative in Figure 3.4 on the metal side. Figure 3.5 shows that the power flow in the transverse direction is toward and into the metal, with the power flow dying off rapidly near the metal's surface. This is consistent with the wave phase fronts being tilted towards the metal interface, and also the physical intuition that since the metal's finite conductivity is the source of the power loss, that the wave's power should flow into the metal and be dissipated there near the surface.

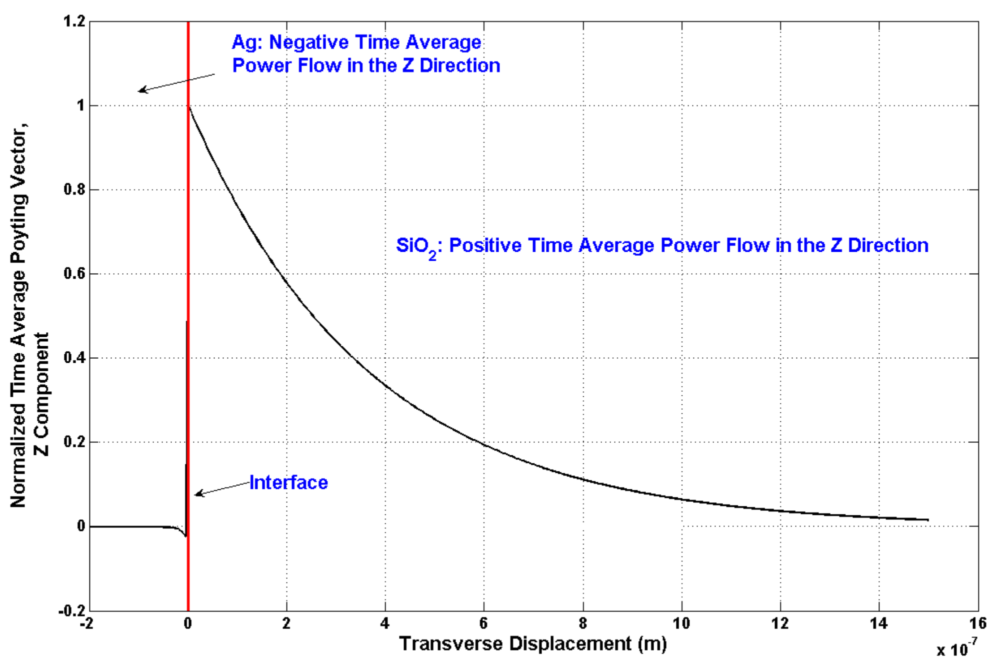

Figure 3.4: Z-component of the time average Poynting vector as a function of transverse displacement for the example outlined above.

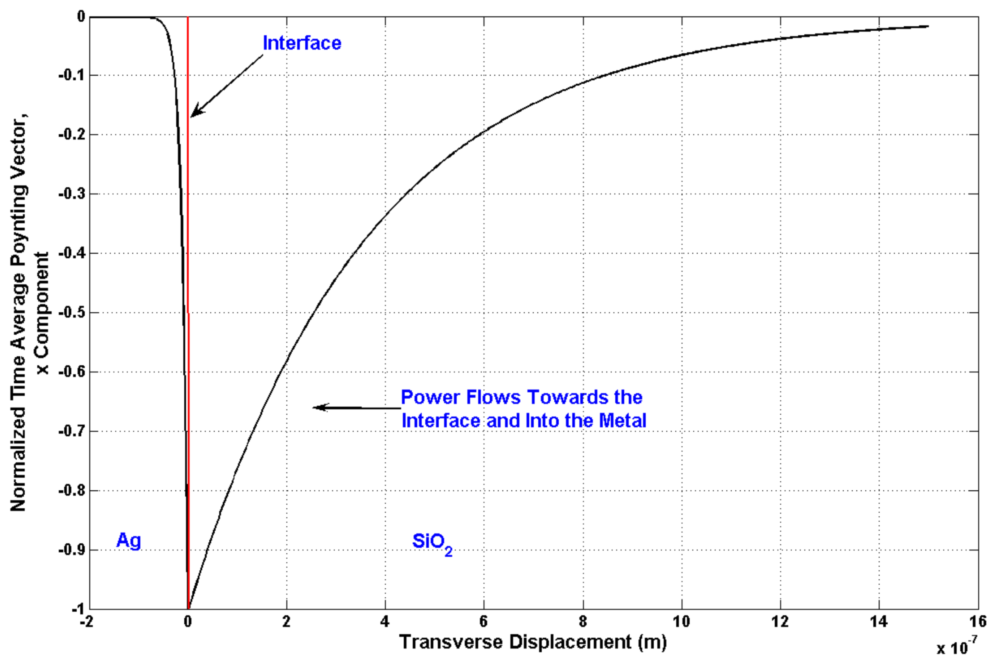

Figure 3.5: X-component of the time-average Poynting vector as a function of transverse displacement for the example outlined above.

3.3: Trends of Propagation Characteristics

Now that a thorough treatment of a specific waveguide has been covered, it is useful to see how the propagation changes as a function of some of the input parameters, namely the bounding dielectric index and the free space wavelength. Below in Figure 3.6 is plotted the transverse decay lengths (also known as skin depth, for metals) of the wave into the metal and dielectric as a function of the dielectric refractive index, here called "n", for Ag and Au at $\lambda_0 = 1.55\ \mu m$. One interesting feature is that the skin depths into Ag and Au are essentially invariant over this n range and remain at about 20 nm, with the Au skin depth being slightly higher. Another interesting feature of these data is that the transverse decay length of the surface plasmon actually increases for *n*'s less than about 1.5. This would imply that if n was decreased below 1.5 that the decay length would decrease, leading to a greater localization of the wave near the interface. Given that most microelectronic processing technologies use silicon dioxide as a dielectric (n = 1.44) or other dielectrics with higher indices (GaAs for instance), and not air, *n*'s less than about 1.5 are not of much interest. This region may be interesting in biosensor applications, however, since the index of refraction of water is 1.33. The general trend above n = 1.5 is for the decay length to decrease and the wave to become more localized to the interface with increasing n. It is a general design goal to increase the localization of the wave at the interface for compact circuitry. However, increasing the localization at the interface comes at the price of decreasing the propagation length of the wave. The propagation length is defined in this chapter as the length at which the amplitude of the field decays to 1/e its initial value.

See Figure 3.7 below for the propagation length as a function of n. One can see that increasing n from 1.5 to 2 has the effect of decreasing the propagation length by about one third for both Ag and Au, while increasing the confinement by about 12 %. At this wavelength, the wave on the Au surface travels further by about 50 microns.

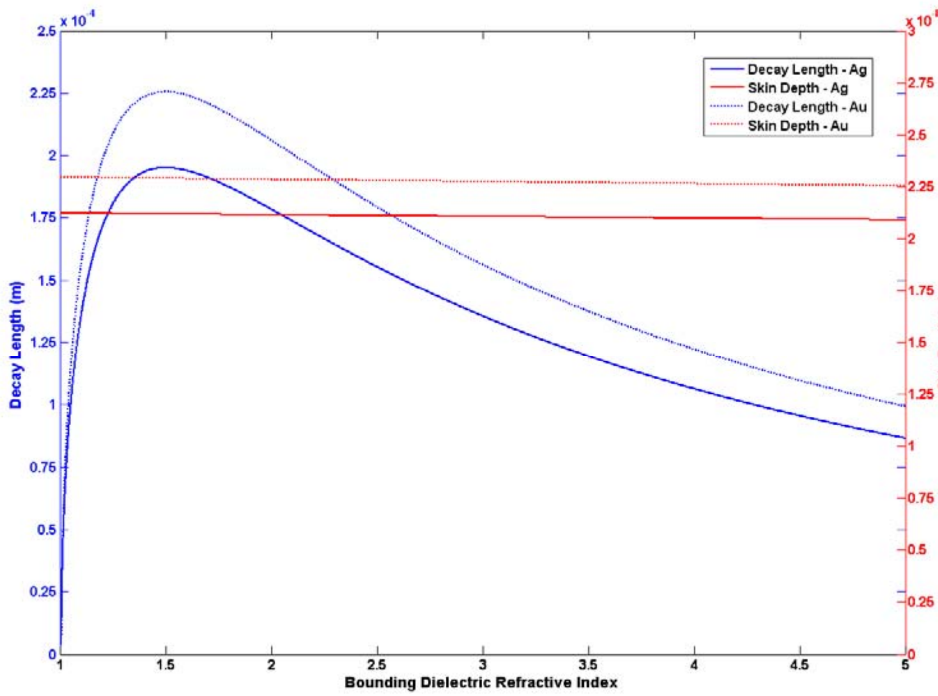

Figure 3.6: Transverse decay length (into dielectric) and skin depth (into metal) of a plasmon surface wave as a function of the dielectric refractive index at free space wavelength of 1.55 um. The left vertical axis is in 10^{-4} meter units, whereas the right vertical axis is in 10^{-8} meter units.

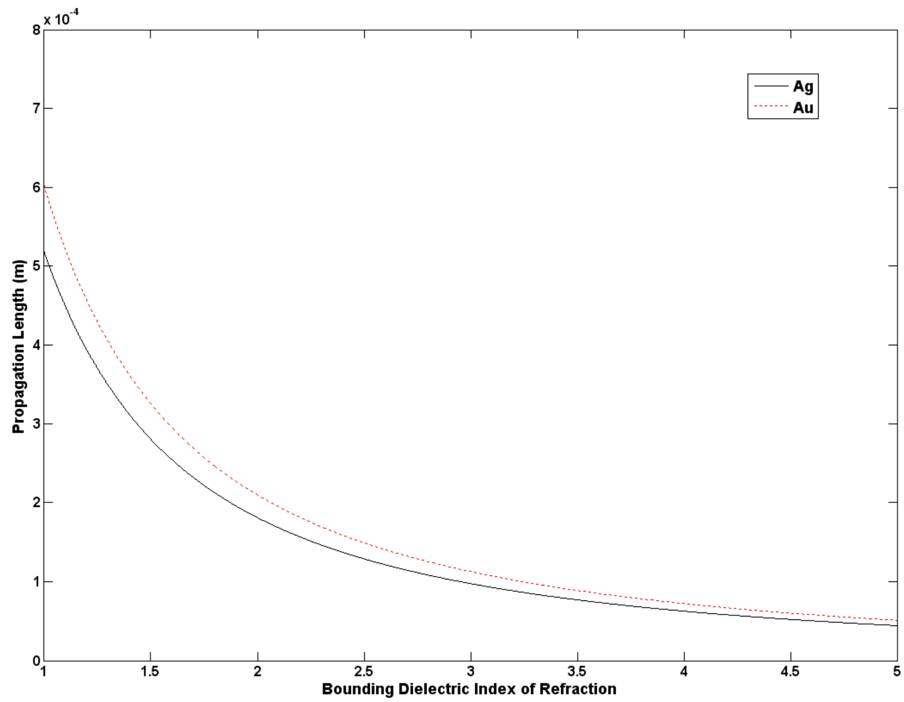

Figure 3.7: Propagation length of a plasmon wave traveling at a metal-(Au and Ag) dielectric interface versus the bounding dielectric index of refraction. The vertical axis is in 10^{-4} m units.

Finally, it is always instructive to look at the dispersion relationship. Figure 3.8 plots the real an imaginary dispersion relationships for an air-Ag interface, plotted using Equation 3.1.7. One can see three regions of operation in Figure 3.8a. In the bound region, the propagation constant of the plasmon is greater than that of the free space wave vector, and so remains localized at the surface. In the radiative region, the propagation constant is less than the free space wave vector, which implies that the transverse wave vectors are now mostly real, which corresponds to radiation away from the interface.

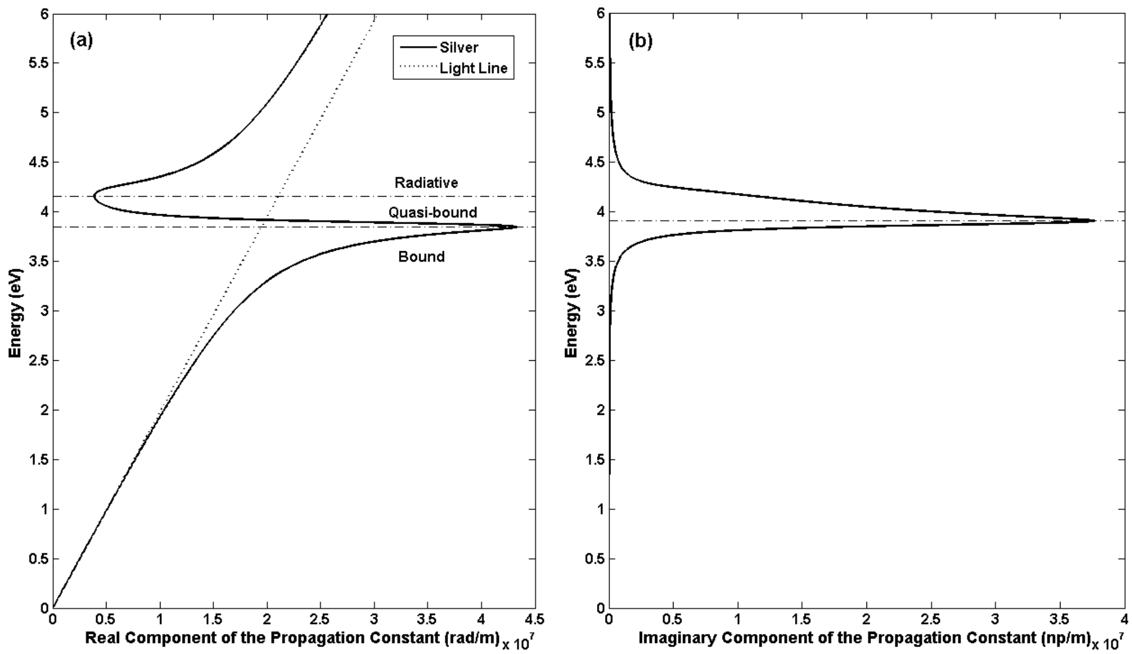

Figure 3.8: Energy versus the real (a) and imaginary (b) parts of the *z* component of the propagation constant for an Ag-air interface. Also, the light line (dot line) for this system is plotted, along with the propagation boundaries (dash-dot in (a)). In (b), the horizontal dash-dot line corresponds to the energy with the smallest propagation length. The Drude model was used for the permittivity of Ag, with parameters from Nordlander-Oubre [29].

The so-called 'quasi-bound' region is effectively a surface plasmon bandgap due to the spike in the attenuation constant (the imaginary part of the propagation constant) in this region, whereby the wave effectively does not propagate [23]. Note also that since the real part of the propagation constant is greater than that of free space in the bound region, it is impossible for one to excite this mode by simply shining TM polarized light at the surface, at any real angle. The angle of incidence is actually complex, which implies that an evanescent wave must be used to excite the mode. In practice, modes are generated on thin metal films, which corresponds to a dielectric-metal-dielectric geometry (not discussed in this thesis), by using a technique called attenuated total reflection (ATR) [35].

3.4: Key Points

In this chapter, the conditions for the propagation of electromagnetic radiation at a single interface between two semi-infinite regions, one being a dielectric, the other being a metal, was derived. It was found that, in order for a surface mode to propagate, the light must be polarized such that the magnetic field is along the interface, which is the so-called transverse magnetic polarization. Also, the real part of the relative permittivity of the metal must be negative and have a magnitude greater than the relative permittivity of the dielectric. The plane wave solution at the interface with the reflection coefficient set to zero leads to a field solution whereby evanescent decay occurs away from the interface on both sides. The wave decays in the direction in which it propagates and has wave fronts tilted towards and into the metal. The transverse time-average power flow is also pointed into the metal. The power flow in the direction of propagation is positive in the dielectric, but negative in the metal. Increasing the refractive index above some size results in the wave becoming more confined near the interface, but also decreases the propagation length of the wave. The dispersion relationship for the wave shows that the propagation constant in the bound region is greater than that which could be excited by a plane wave, which indicates that an incident evanescent field must be used to excite the surface mode. Though this case is highly ideal, the valuable insights it can provide are generalizable to more complex waveguiding structures.

Chapter 4: Guiding Light in a Dielectric Gap between Two Semi- Infinite Metal Regions

4.1: Analytical Solution for the Two Dimensional Slab Waveguide

The single interface equation above is of limited practical use as coupling light to it requires an incident wave that is evanescent. In this chapter, the ideal two dimensional slab waveguide will be discussed, for the case where the slab is a dielectric surrounded on either side by a metal, forming two metal-dielectric interfaces. This is the so-called metal-insulator-metal (MIM) slab structure [36]. The same sort of two-dimensional plane wave analysis can be done to derive the Fresnel reflection coefficients for this type of structure, and the waveguide's characteristic equation can be derived from this coefficient by setting it to zero. Only the TM polarization will be discussed. Kaminow showed that TE polarized waves have much shorter propagation length (by about two orders of magnitude) in the MIM geometry for the subwavelength slab widths studied [18]. The characteristic equation for this is given below, which was derived by applying the boundary conditions for a plane wave solution at both interfaces:

$$F(n_{eff}) = \frac{\left\{ m\cdot\pi + \arctan\left[\frac{\varepsilon_2}{\varepsilon_1}\cdot\sqrt{\frac{\left((n_{eff})^2 - \varepsilon_1\right)}{\left(\varepsilon_2 - (n_{eff})^2\right)}}\right] + \arctan\left[\frac{\varepsilon_2}{\varepsilon_3}\cdot\sqrt{\frac{\left((n_{eff})^2 - \varepsilon_3\right)}{\left(\varepsilon_2 - (n_{eff})^2\right)}}\right]\right\}}{\sqrt{\left(\varepsilon_2 - (n_{eff})^2\right)}} - a\cdot k_0 = 0 \qquad (4.1.1)$$

Here, $\varepsilon_1, \varepsilon_2$ and ε_3 are the dielectric constants of the three regions, with the first and third regions being semi-infinite regions on either side of the second region (the slab or core) with finite width a. The parameter n_{eff} is the effective mode propagation index, which is defined as the propagation constant of a guided mode normalized to the free space propagation constant. The term m is the mode number, where $m \geq 0$ and m is an integer, and determines the number of transverse zero-crossings of the mode. For the case of plasmon propagation, n_{eff} is a complex number. The zeros of the transcendental equation, $F(n_{eff})$, have been solved over the complex plane by using the Nelder-Mead simplex method to minimize its complex magnitude [37]. Since the waveguide studied in this chapter is symmetric around the slab, it represents a special case of Equation 4.1.1:

$$F(n_{eff}) = \frac{\left\{ m \cdot \pi + 2 \cdot \arctan\left[\frac{\varepsilon_c}{\varepsilon_m} \cdot \sqrt{\frac{\left((n_{eff})^2 - \varepsilon_m\right)}{\left(\varepsilon_c - (n_{eff})^2\right)}} \right] \right\}}{\sqrt{\left(\varepsilon_c \quad - \quad (n_{eff})^2\right)}} \quad - \quad a \cdot k_0 = 0 \qquad (4.1.2)$$

Here, ε_c is the relative permittivity of the dielectric core, and ε_m is the permittivity of the metal cladding.

4.2: Propagation Characteristics as a Function of Slab Width

Below in Figure 4.1 is plotted the real component of the effective propagation index as a function of core width for the Ag-Polymer-Ag slab waveguide at a wavelength of 0.633 microns. The polymer is the one specified by Kaminow, with a dielectric constant of 2.523. Also are plotted data directly from Kaminow's paper as a comparison. One can see that the Kaminow data matches up with that determined using Equation 4.1.2 well. The first observation to make on these data is that TM_0 does not experience a cutoff width over this width range, whereas all of the other modes do. The propagation constant of this mode actually increases with a smaller geometry and the mode becomes *more* confined, well above the light line for the medium and the effective index of the single interface. Mode TM_1 is able to obtain a propagating wave vector with a magnitude greater than a plane wave in the polymer, but it does not display increasing confinement with a thinner slab. One can also see that modes TM_0 and TM_1 are asymptotic to the effective propagation index of the single interface for larger slab widths, indicating that the localization of the field's energy at the metal-insulator interfaces rather than the core. The higher order modes asymptotically approach the light line of the polymer, which is expected since waves that have more than one transverse 180 degree phase shift most likely have most of their propagating power within the core, away from the influence of the metal. The vertical dashed line in the figure is the boundary for subwavelength confinement, using Equation 1.1.1. Only the fundamental mode (TM_0) is above the light line for widths below this boundary. It is interesting to note that TM_0 and TM_1 are both able to have propagation constants greater than the free space wavevector, which is something one would never see in a dielectric waveguide.

The reason for the limiting behavior of TM_0 for smaller slab widths can be seen from Equation 4.2.1, setting *m* equal to zero, and for simplicity assuming that the dielectric constant of the metal is purely real and negative:

$$a = \frac{-2 \cdot \arctan\left[\frac{\varepsilon_c}{|\varepsilon_m|} \cdot \frac{\gamma_x}{k_x}\right]}{k_x} \tag{4.2.1}$$

where

$$k_x \overset{\Delta}{=} \text{transverse slab core wavevector} = k_0 \cdot \sqrt{\left(\varepsilon_c - (n_{eff})^2\right)} \tag{4.2.2}$$

$$\gamma_x \overset{\Delta}{=} \text{transverse metal cladding decay constant} = \sqrt{\left((\varepsilon_c - \varepsilon_m)k_0^2 - k_x^2\right)} \tag{4.2.3}$$

Given that n_{eff} is real and positive (for a propagating wave), and that γ_x is positive and real (for a confined wave), k_x cannot be real since this would force the width of the waveguide, a, to be negative, which is unphysical. Therefore, k_x must be imaginary:

$$a = \frac{-2 \cdot \arctan\left[\frac{\varepsilon_c}{|\varepsilon_m|} \cdot \frac{\gamma_x}{i \cdot |k_x|}\right]}{i \cdot |k_x|} \tag{4.2.4}$$

then using

$$\arctan(-i \cdot y) = -i \cdot \operatorname{arctanh}(y) \tag{4.2.5}$$

results in the following equation:

$$a = \frac{2 \cdot \operatorname{arctanh}\left[\frac{\varepsilon_c}{|\varepsilon_m|} \cdot \frac{\gamma_x}{|k_x|}\right]}{|k_x|} \tag{4.2.6}$$

This equation now has possible solutions for n_{eff} through k_x. It now remains to be shown that when the width decreases, the magnitude of k_x increases. This requires knowledge of the inverse hyperbolic arctangent for a positive argument: for arguments less than 1, arctanh increases from zero and asymptotically approaches infinity at one. For arguments greater than one, arctanh decreases from infinity and approaches zero. Because the waveguide width must remain a finite number, the argument of arctanh must be either greater than or less than 1. A limiting case is enough to determine the proper region. Substituting in the definition for γ_x in Equation 4.2.6 and distributing yields the following:

$$a = \frac{2 \cdot \operatorname{arctanh}\left[\frac{\varepsilon_c}{|\varepsilon_m|} \cdot \sqrt{1 \quad + \quad \frac{k_0^2 \cdot (\varepsilon_c + |\varepsilon_m|)}{|k_x|^2}} \right]}{|k_x|} \tag{4.2.7}$$

Then as $|k_x|$ goes to infinity, the argument of the artanh function goes to a constant value less than one due to the requirement (discussed in the previous chapter) that the core refractive index be less than the magnitude of the metal's index. This means that the argument of the arctanh function is always less than one and that the arctanh function is a positive function over this section of its domain. As $|k_x|$ increases, therefore, the right side of Equation 4.2.7 must decrease and so too must the slab height. The magnitude of k_x is related to the effective index by the Pythagorean Theorem:

$$n_{eff} \quad = \quad \sqrt{\varepsilon_c + \left(\frac{|k_x|}{k_0} \right)^2} \tag{4.2.8}$$

And so the effective index must increase along with the transverse core wavevector, as the slab height decreases. This behavior is true of mode 0, but not of the other modes, because the presence of the constant multiple of π in the numerator (see Equation 4.1.2) allows k_x to be real (i.e. transverse oscillations in the core). This relationship was derived for the simple case where the metal is lossless, but it is clearly also true when the imaginary component of ε_m is small. Unfortunately, this explanation relied on the relationship between the wavevector and the characteristic equation, and is not applicable to physically-realizable structures like rectangular waveguides for which an analytical solution does not exist. However, one still does observe that the effective propagation index increase for the three-dimensional (finite height) plasmonic gap waveguide for modes that have no transverse 180˚ phase flips in a given direction. This will be shown in the next chapter.

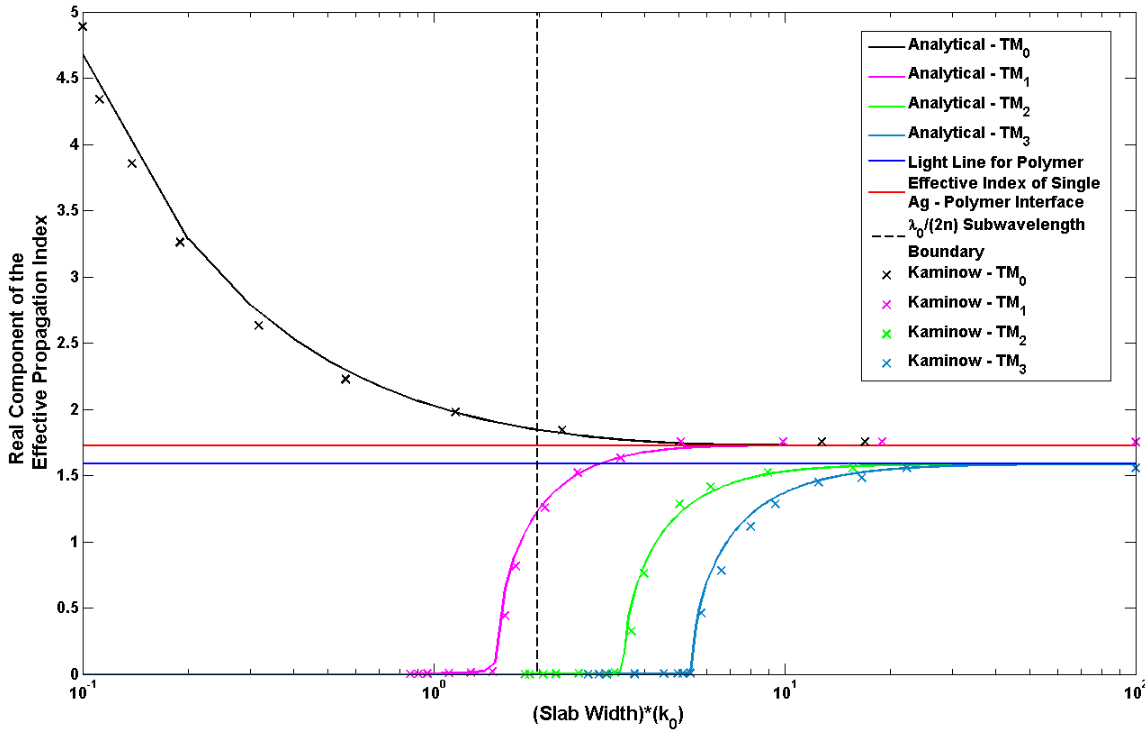

Figure 4.1: Real part of the complex propagation index versus the product of slab width and free space wavevector for four TM modes: Analytical solution from the author and Kaminow. The width was swept while holding the free space wavelength at 633 nm.

In Figure 4.2 below, the power propagation length is plotted below. The power propagation length is defined here as the length over which the power carried by the wave decays to 1/e its initial value:

$$L_{Prop} = \frac{\lambda_0}{4\pi \cdot \mathrm{Im}\{n_{eff}\}} \tag{4.2.9}$$

The values from Kaminow's paper don't seem to match up as well here, but the article [18], which had been scanned-in by the publisher, was at a slight tilt angle, making "Windows Paint Data Point Acquisition" much less accurate. It can be seen however, that Kaminow's values track the analytical ones in their shape. In this figure, one sees that over the slab widths of interest (again, to the left of the dashed subwavelength boundary, where plasmonic waveguides have the advantage over dielectric waveguides) TM_0 has a propagation length more than three orders of magnitude higher than any of the other modes besides TM_1 for slab widths near the boundary. This, along with the above observation that the fundamental mode becomes more confined at smaller widths makes it the primary mode of interest for waveguiding purposes. It is interesting to note that it is actually TM_2 that has the lowest loss of all the modes for very large widths. Again, TM_0 approaches the loss of the single interface for large widths, indicating that the two waves at each metal-insulator surface become decoupled from each other for a wide enough waveguide. Finally, for all modes, decreasing the slab width decreases the propagation length, which is another manifestation of the tradeoff between confinement and loss. The higher order modes experience a sharp increase in the loss at some point, and this occurs at the corresponding "cutoff width" for the mode in Figure 4.1, where Re(n_{eff}) goes to zero.

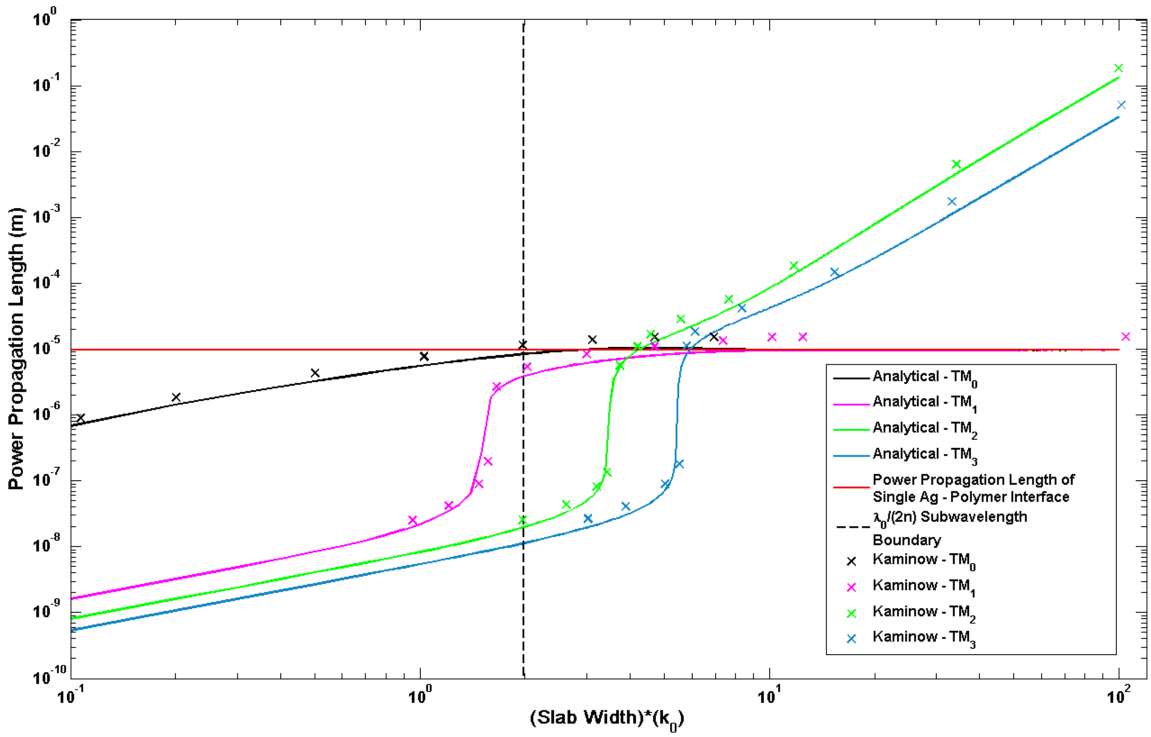

Figure 4.2: Power propagation length versus the product of slab width and free space wavevector for four TM modes: Analytical solution from the author and Kaminow. The width was swept while holding the free space wavelength at 633 nm.

4.3: Field Solutions

For the slab waveguide, the x-dependent solution form for the y-component of the magnetic field is given by the following piecewise equation:

$$H_y(x) = \begin{cases} \cos\left(\frac{k_x \cdot a}{2} - \varphi\right) \cdot e^{-\gamma_x\left(x - \frac{a}{2}\right)}, & \text{for } x > \frac{a}{2} \\ \cos(k_x \cdot x), & \text{for } |x| \le \frac{a}{2} \\ \cos\left(\frac{k_x \cdot a}{2} + \varphi\right) \cdot e^{\gamma_x\left(x + \frac{a}{2}\right)}, & \text{for } x < -\frac{a}{2} \end{cases} \tag{4.3.1}$$

where

$$\varphi = \frac{m \cdot \pi}{2} \tag{4.3.2}$$

Here, m here is the mode number [39]. The field distributions are plotted below in Figure 4.3 for the four different modes shown above in Figures 4.1 and 4.2, with a slab width of 1 μm. It is assumed here that the amplitude of the field is 1. Observed here is what is expected: the mode number gives the number of zero crossings, which are 180˚ phase shifts, in the transverse direction. All of the modes display some kind of field enhancement near the interfaces. For TM_0 - and TM_1, however, the magnitude of the field at the boundaries is the peak amplitude, whereas for the higher order modes, the peak field amplitude is within the core of the waveguide. As far as confinement is concerned, the modes have visibly similar skin depths into the metal.

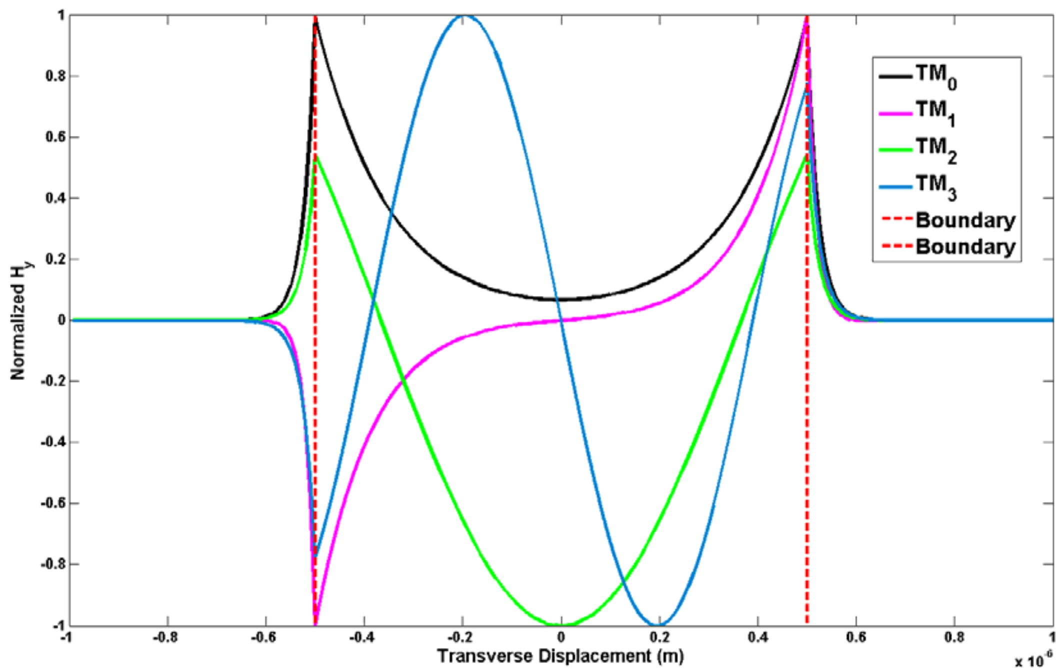

Figure 4.3: Mode profiles (y component of the magnetic field) for the Ag-polymer-Ag gap waveguide studied by Kaminow with a gap width of 1 μm: modes TM_0 through TM_3.

The phase of these waves is also of interest. Figure 4.4 shows the transverse phase distribution of the y-component of the magnetic field for the first three modes. One sees that the phase of the waves changes by 180˚ the proper number of times for each mode. Unlike a dielectric waveguide though, the phase fronts are tilted and do no transition instantaneously (especially for TM_2). In the metal, the phase decreases away from the interfaces. Because this field distribution was taken at a fixed time, the changing phase is due only to spatial oscillation. Incrementing the time would increase the phase by a constant across the transverse profile, whereas incrementing spatial displacement in a direction in which the wave is travelling will decrease the phase. Because the spatial phase is decreasing away from the interface, the wave must be radiating in the direction away from the interface, which is again consistent with the analysis in the previous chapter, that all plasmon waves are fundamentally radiative, into the metal, because of the finite conductivity. One can also see that the phase of the waves decreases away from the center of the waveguide (transverse displacement = 0 m) which says that the wavefronts in the dielectric are tilted towards the metal, and this is consistent with the single interface case where the same occurred. It is useful to know that the easily-solved cases can provide insight into the behavior of the more complicated ones.

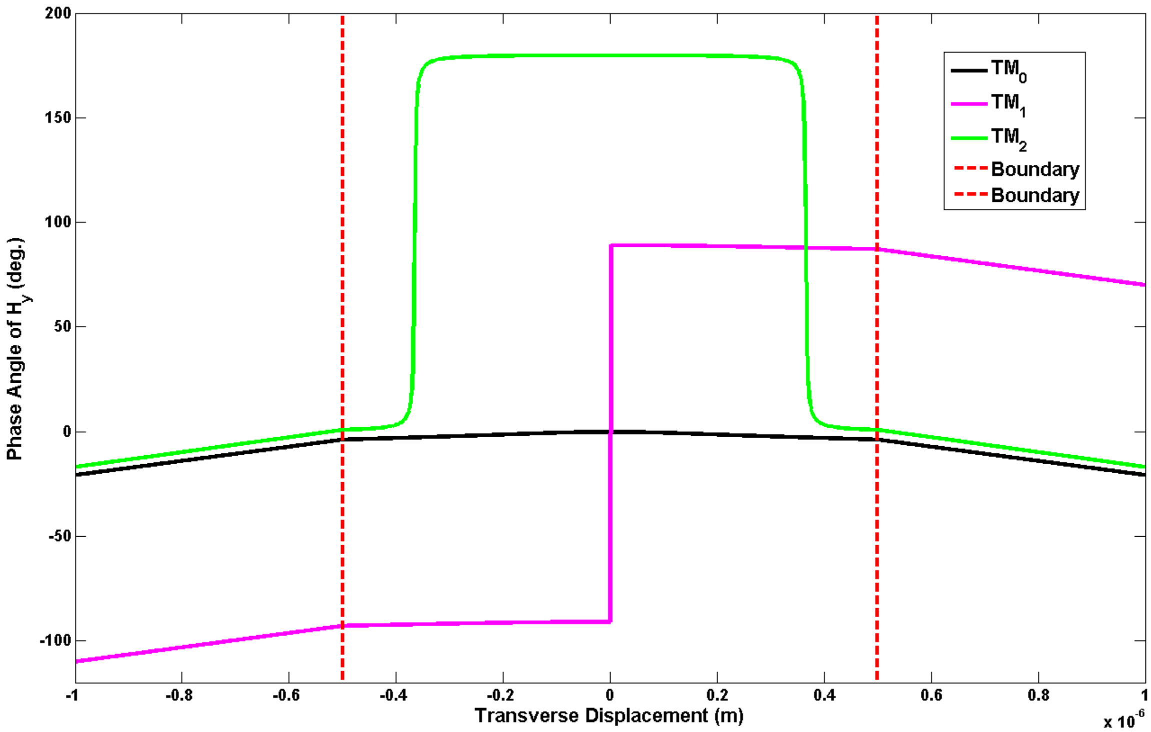

Figure 4.4: Transverse phase distribution of the first three modes of the Ag-polymer-Ag gap waveguide studied by Kaminow, for a gap width of 1 μm.

The distribution of the three field components, H_y, E_z, and E_x, is shown below in Figure 4.5 for mode TM_0. This was plotted using Equation 4.3.1 along with the spatial phase (propagation) constant in the Z-direction, using *MATLAB™*. The distribution of the magnetic field is as one would expect given Figure 4.3, but the electric field has some interesting features. Here, the electric field alternates between pointing in the positive and negative *x*-direction as the wave propagates. This is why the fundamental mode of the plasmon gap is often referred to as the "capacitor mode [40]." Although it is a bit difficult to tell, the electric field here also displays the same divergence behavior at the interface at locations along the *z*-direction.

4.4: Exploring the Relationship between Confinement and Loss

The purpose of this final section is to try to explain why increasing the confinement of the light (decreasing the slab width) causes the propagation length to decrease (or equivalently, the imaginary component of the propagation index to increase). For this, one can use the power relationships for the TM case that was derived on the first midterm exam in the ECE 694H class [41]. The formulas are given below:

$$P_{core} = \left(\frac{k_0 \cdot n_{eff}}{2 * \omega * \varepsilon_c}\right) * \left(a + \frac{\sin(k_x * a) * \cos(k_x * a)}{k_x}\right) \tag{4.4.1}$$

$$P_{metal} = \left(\frac{k_0 \cdot n_{eff}}{2 * \omega * \varepsilon_m}\right) * \left(\frac{(\cos(k_x * a))^2}{\gamma_x}\right) \tag{4.4.2}$$

$$\Gamma_{metal} = \frac{|\operatorname{Re}\{P_{metal}\}|}{|\operatorname{Re}\{P_{metal}\}| + |\operatorname{Re}\{P_{core}\}|} \tag{4.4.3}$$

Here, P_{core} is the power contained in the core, P_{metal} is the total power in the metal claddings on both sides of the core. The quantities γ_x and k_x are as defined above for equations (4.2.2) and (4.2.3). The parameter Γ_{metal} is of course the proportion of the wave's time average propagating power contained in the metal cladding.

Figure 3Figure 4.5

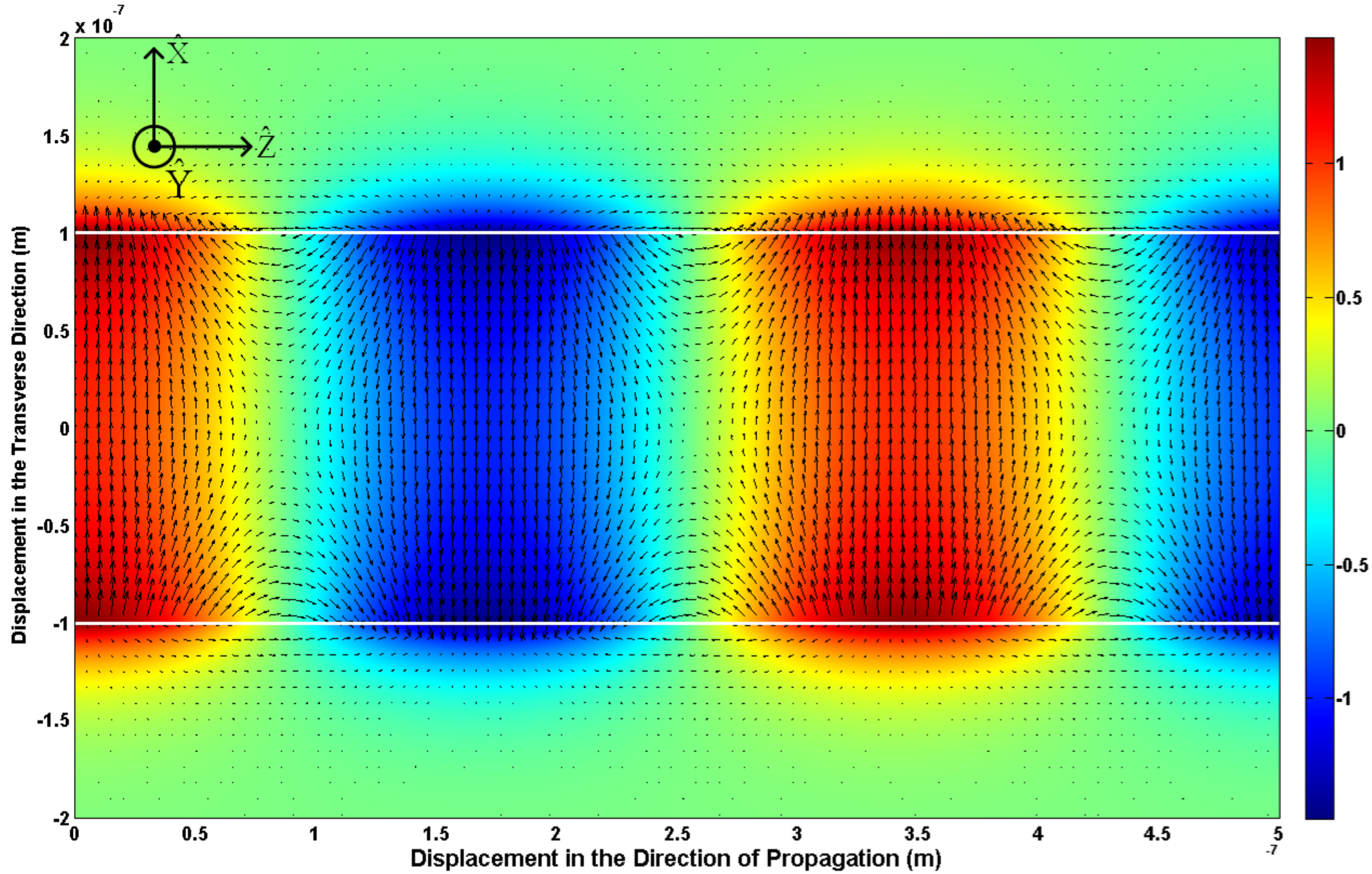

Figure 4.5: Color plot of H_y and arrow plot of E showing the spatial distribution of the fields. The white lines show the boundaries of the dielectric slab.

Plotted in Figure 4.6 is Γ_{metal} versus the propagation length of the wave for increasing values of waveguide width (varied implicitly as a parameter), and a fixed core index. This is an extremely interesting result, because it shows that increasing the confinement of the light by making the core width smaller has the effect of causing a greater proportion of the wave's propagating power to be stored in the metal, which, due to the dissipation of this power by means of electron collisions in the metal, means that the loss should be higher. Plotted in Figure 4.7 is Γ_{metal} versus propagation length for an increasing core index (the implicit parameter here) at a fixed core width. One can see here the same trend: that increasing the core index tends to increase the proportion of the power confined in the metal and decrease the propagation length.

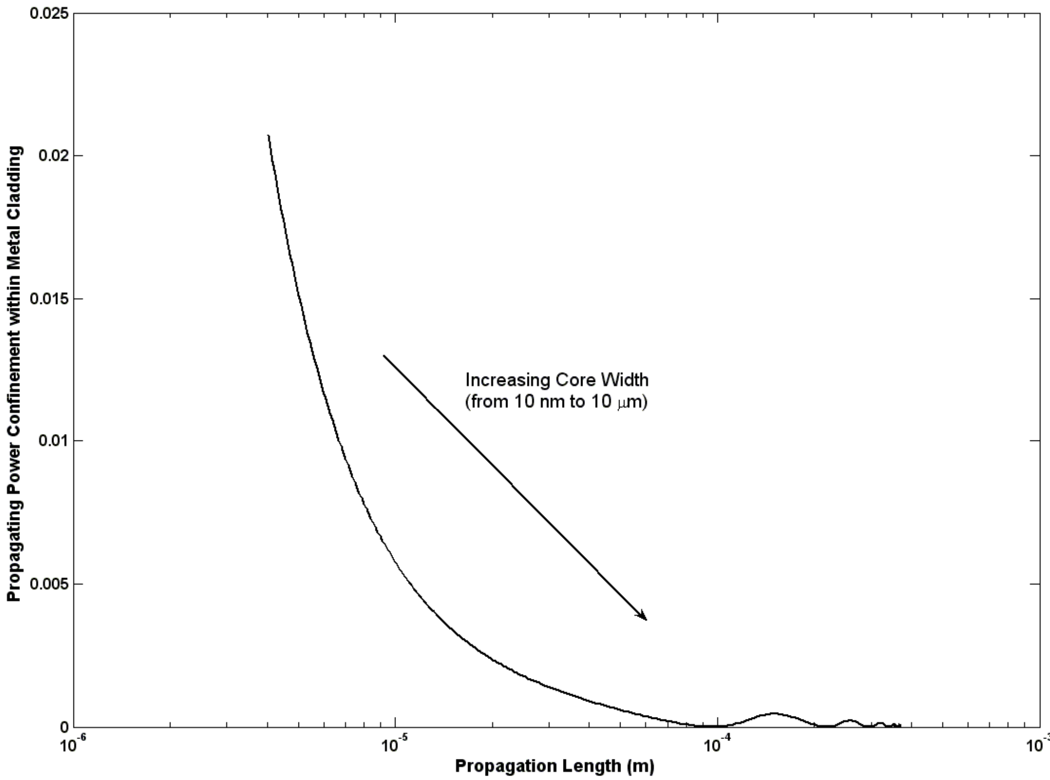

Figure 4.6: Propagating power confinement within metal cladding versus TM_0 propagation length for increasing core widths, for an Au-$Si0_2$-Au slab waveguide at a 1.55 µm free space wavelength. Here, the index of refraction of $Si0_2$ is assumed to be 1.444.

A curious feature of this plot (and to a lesser extent, Figure 4.6) are the oscillations of the power confinement with the value of the implicit parameter. There evidently seem to be combinations of waveguide parameters that result in almost a zero confinement of the wave's power in the metal while still remaining at a finite propagation length.

Another, final, figure of merit exploring the tradeoff between confinement and loss is similar to the ones above, but instead of looking at the propagating power within the metal cladding, it looks at the sum transverse decay lengths (surface mode width) away from one of the metal-dielectric interfaces, as if the other interface did not exist. This gives an indication on how localized the power of the wave is at the surface.

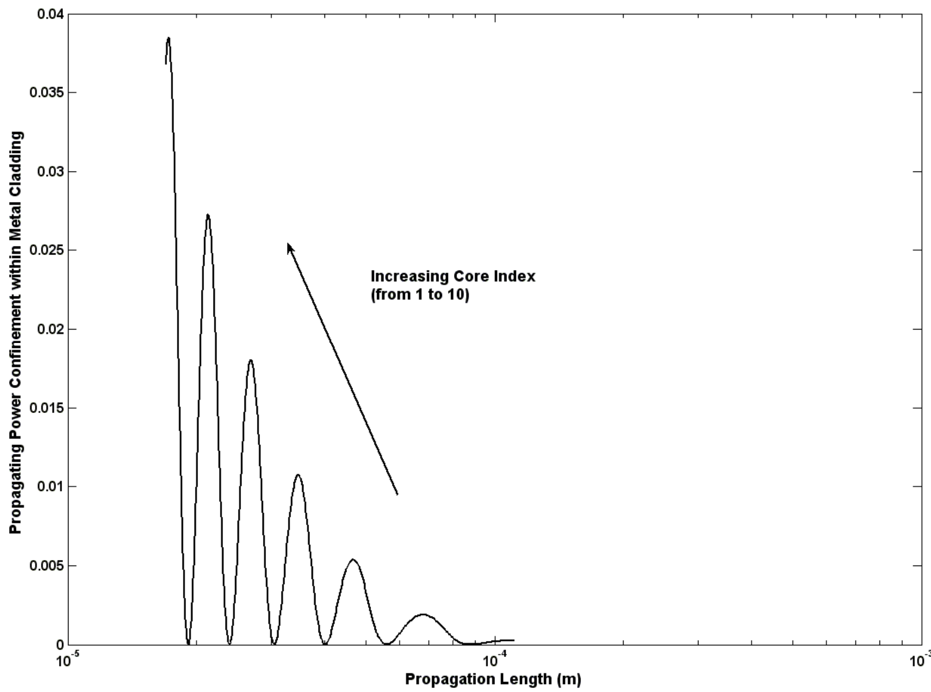

Figure 4.7: Propagating power confinement within metal cladding versus TM_0 propagation length for increasing core indices, for a Au-dielectric-Au slab waveguide at a 1.55 µm wavelength, and a width of 0.5 µm.

The surface mode width, *W*, was calculated from the equation below:

$$W = \frac{1}{|\mathrm{Im}\{\gamma_x\}|} + \frac{1}{|\mathrm{Im}\{k_x\}|} \tag{4.4.4}$$

This is plotted below in Figure 4.8. This shows that as the core width is decreased, the localization of the wave near the surface increases (surface mode width decreases). Again, given that the charge is oscillating at the surface of the metal where loss occurs, if a greater proportion of the wave's power is concentrated here, the loss will be greater.

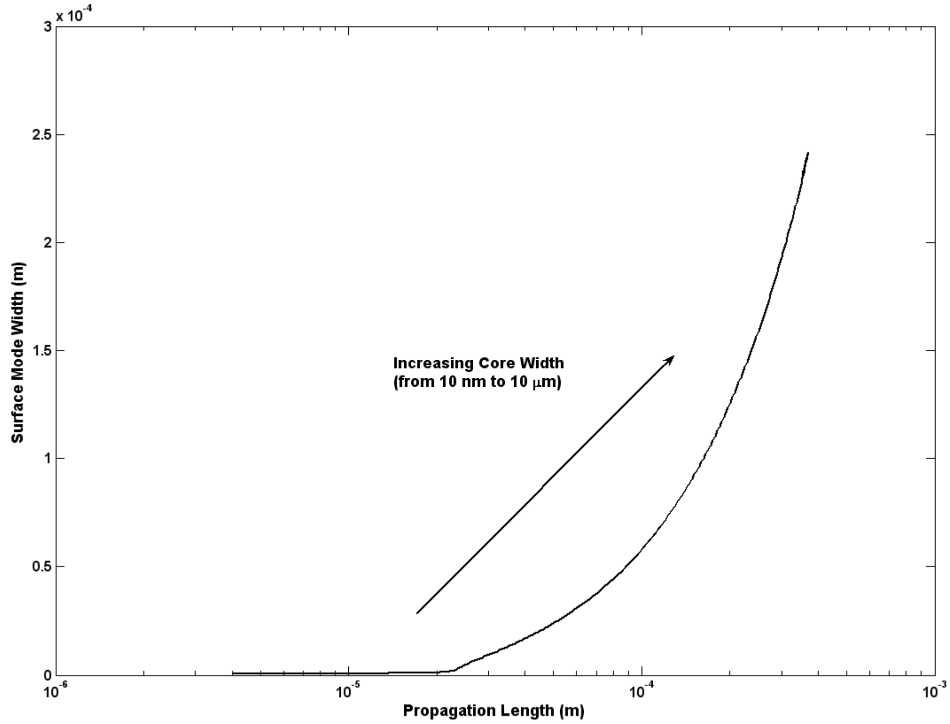

Figure 4.8: Surface mode width versus TM0 propagation length for an increasing core width, with a core index of 1.444, and Au cladding at a free space wavelength of 1.55 μm**.**

4.5: Key Points

The propagation characteristics, field distributions, and trends of transverse magnetic polarized electromagnetic energy propagating in the metal-dielectric-metal two-dimensional slab waveguide at optical and near infrared frequencies were explored in this chapter. The complex propagation constant was determined by solving the well-known two-interface slab waveguide characteristic equation over the complex plane using the Nelder-Mead simplex method as implemented in *MATLAB*™. First, the complex propagation constant was plotted as a function of slab width using parameters from Kaminow's paper. It was found that the higher order modes (TM_1, TM_2, TM_3, etc.) exhibit a cutoff width and cease to propagate, whereas the fundamental mode (TM_0) actually becomes more confined, with the real part effective propagation index ($\mathrm{Re}(n_{eff})$) increasing at an increasing rate for low widths. For both TM_0 and TM_1, $\mathrm{Re}(n_{eff})$ asymptotically approaches that of the single interface case for large widths, indicating a decoupling of the plasmon waves at each of the interfaces. For slab widths corresponding to subwavelength confinement (as defined by Equation 1.1.1 above), only TM_0 has any significant propagation length and level of confinement. As expected, the propagation length of all of the modes decreases as the slab width becomes narrower. The field distributions show that the modes have a relative minimum in their field amplitude at the metal-dielectric interfaces. For TM_0 and TM_1, this amplitude is the maximum amplitude of the wave, but the higher order modes have a greater amount of power stored away from the interfaces near the center of the core. The phase fronts of all the modes are tilted towards the interface and into the metal, just as with the single interface case, showing that the power flow is into the metal, where the loss occurs. The electric field distribution of TM_0 is very much like that of a bunch of capacitors in parallel with alternating polarities between adjacent capacitors. A final analysis was done examining the tradeoff between confinement and loss: it was found that as the power of the wave is confined more closely to the surface of the metal, either by increasing the refractive index or decreasing the slab width, the propagation length decreases. It is however interesting to note that there are some slab widths where the power confinement goes almost to zero and yet the power propagation length remains constant.

Chapter 5: Guiding Light in a Plasmonic Gap Waveguide

5.1: The Modes of the Plasmonic Gap

The purpose of this chapter is to examine the modal structure and propagation characteristics of the plasmon gap, the geometry for which is given in Figure 1.2. Unfortunately, unlike the two-dimensional waveguides studied earlier, the mode profiles and propagation constants for this waveguide cannot be solved analytically, because it involves solving the two-dimensional Helmholtz Equation over the transverse (X-Y) plane, an equation the solution for which is non-separable in X and Y in general. Thus, determining the propagation characteristics of this structure involves approximate numerical methods.

The simplest method that has been employed is called the effective index method (EIM) [42]. This is a general method for determining the effective propagation index of planar-rectangular dielectric waveguiding structures, and it assumes that the *X* and *Y* dependencies of the field distribution are separable. This assumption is valid for cases, such as waveguiding with dielectrics, where the field magnitude in the corner regions of the waveguide is negligible, and so it ignores the refractive index distributions in the corners completely. The method works by solving the propagation constant of the corresponding slab waveguide mode in one direction, and then using the resulting effective propagation index as the core index of the slab which is solved in a second direction, normal to the first. This method has shown to produce inconsistent results for the loss of the fundamental mode of the plasmonic gap, which is of course a critical parameter when analyzing metallic waveguiding structures at optical frequencies. Bozhevolnyi (BZ) [40] was able to carry-out such an analysis and publish his work, even though his results go against those of his primary source for comparison [43]. Figure 5.1 below gives the raw data from [40] and [43] as a comparison. In Figure 5.1a, BZ presents his results for the real part of the effective index and the "propagation length" as a function of gap height. He shows that the real part of the propagating wave vector matches up almost exactly with that determined by the finite difference (FD) method used by Han, He, and Liu (HHL) [43]. However, the EIM he was using gives that the propagation length decreases with larger gap heights, whereas the paper to which he was comparing his data [43], shown in Figure 5.1b, gives that a plasmon gap, with a constant gap width, will exhibit an increasing propagation length with increasing gap heights. It is amazing that BZ was able to get his paper published at all with such inconsistent results for the loss in a case where determining the propagation length is critical. This indicates, along with the intuition gained from other simulation methods like the finite element method (FEM), that the key assumption made in using the EIM, that the field amplitude is negligible near and in the corner regions, is incorrect.

A relatively simple numerical method that has been used is the method of lines (MOL) [44]. This was successfully employed by Pierre Berini and others to study metal strip waveguides [45, 46]. This method could have been used for the analysis presented in this paper, but the author did not have enough time to implement it. In the future, this would be a way to check the results of other techniques.

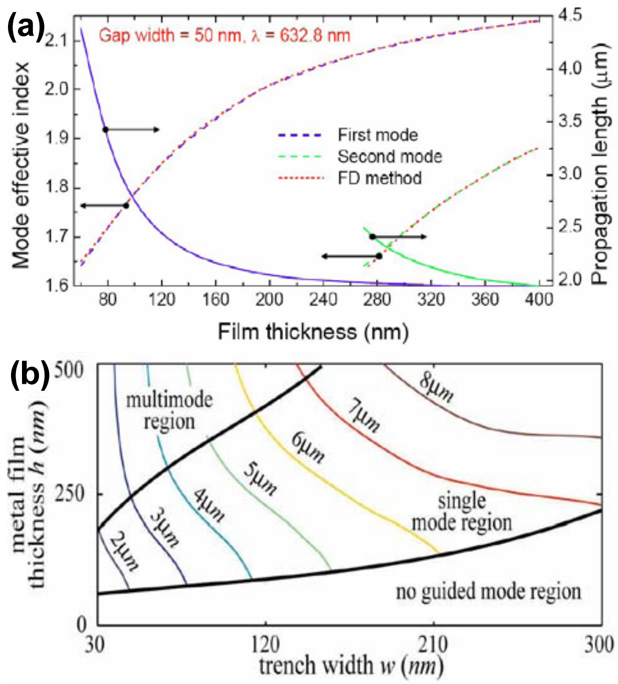

Figure 5.1: Propagation lengths as a function of gap height, *h*: (a) figure taken from Bozhevolnyi [40], who used the finite element method, showing the "propagation length" (solid blue curve) as a function of film thickness (b) figure taken from Han, He, and Liu [43], who used the finite difference method, showing power propagation length contours for the plasmon gap

The primary method that was used in this analysis is FEM. The software package that implements this method, *COMSOL*™, was used for the analysis. The finite difference time domain (FDTD) method was used to check the results of the FEM simulations, which was also implemented as commercial software (*RSoft*™). The details of the specific implementations of the software, or the general implementation of FEM or FDTD, will not be given here. For this analysis, FEM was used as a mode solver to find a solution to the two-dimensional Helmholtz Equation over the transverse plane of the finite-height plasmon gap waveguide structure shown in Figure 1.2. The FDTD method took the resulting field profiles and propagation constants as excitation inputs, and was used for verification. Unfortunately, the computational resources available at the time were not sufficient to obtain converged, stable FDTD results. FEM also has the inconvenient behavior of finding solutions that are not physical (the so-called "spurious solutions"), and so in many cases, manual work must be done to sift out the unphysical modes.

For the absorbing boundary conditions, no PML was used, but rather the built-in "scattering" or radiative boundary condition was used along the simulation boundary. The element type was set to "Vector-Lagrange, Cubic."

To examine the modes that are guided, the waveguide parameters from HHL are used [43], which calls for a cover and core index of 1.49, and a substrate index of 1.47. The metal is Ag (with an index of 0.119 – i*3.964), and the free space wavelength is 632.8 nm. The gap width is 50 nm with a varying height. First, the field profiles for the case when the gap height is also 50 will be examined. Below in Figure 5.1 is shown the meshing and refractive index distribution used in simulation. One can see here that the mesh is much denser near the two vertical metallic sidewalls of the gap. To obtain this, the maximum element size near the sidewalls was set to 1 nm, and the element growth rate (EGR), which specifies the maximum rate at which adjacent mesh elements can grow, was set to 1.1. This corresponds to a maximum 10 % growth rate between adjacent mesh elements. The inset shows the coordinate system, with the *Z* direction being the direction of propagation, and the *X* and *Y* directions defining the transverse plane.

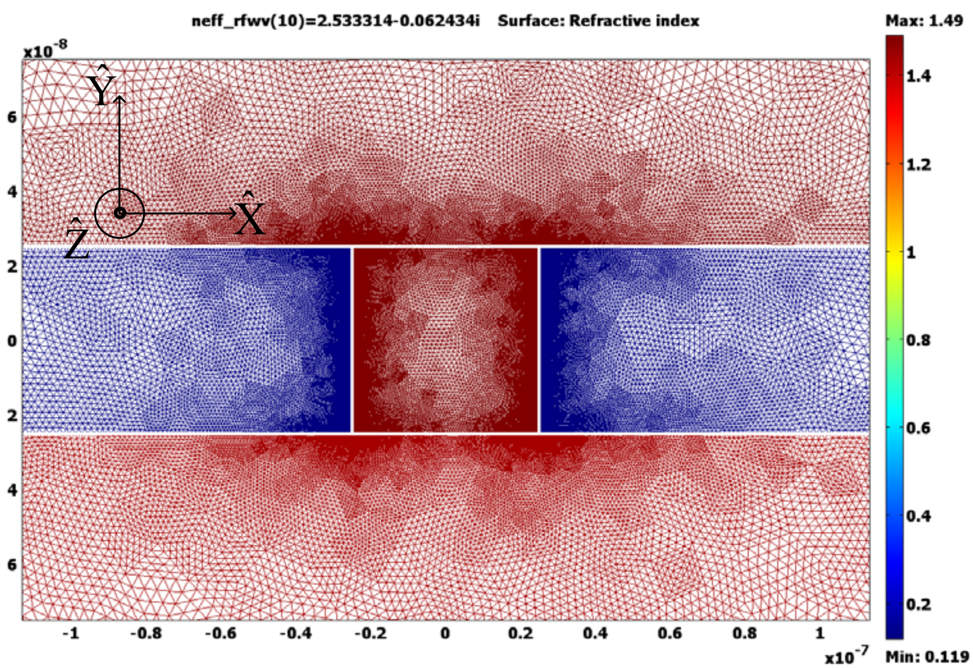

Figure 5.1: The color plot gives the distribution of the real part of the refractive index, generated using the *COMSOL*™ commercial FEM package**.** The white lines denote the region boundaries, with the blue regions corresponding to the silver film, and the reddish ones the dielectric. The mesh is shown with triangular sections. Note the inset which shows the coordinate system.

As was discussed in previous chapters, the plasmon wave only exists when the light is polarized such that the primary component of the magnetic field is tangential to the metal-dielectric interfaces of the waveguide, which in this case are the vertical metal sidewalls. Therefore, the electric field should be polarized in the *X* direction. The modes will be labeled according to Marcatili's convention for the hybrid modes of rectangular waveguides as E^{x}_{pq}, where the superscript *x* denotes the direction of polarization, the first subscript index, *p*, gives the number of intensity peaks of the primary (polarization direction) component of the electric field in the *X* direction, and the second subscript index, *q*, gives the same in the *Y* direction [47]. The mode E^{x}_{11} is also called the fundamental mode of the waveguide.

Figures 5.2a, 5.2b, and 5.2c show the magnetic, electric, and time average power flow (time average Poynting vector) plots for mode E^{x}_{11}, respectively, generated with the COMSOL Multiphysics™ software. Note that the field intensities shown here are arbitrary, and only relative amplitude changes are important here. For the magnetic field distribution, one can see that, as required, the polarization-defining component, H_y of the magnetic field is tangential to the vertical metal sidewalls of the gap. This component also has its largest intensity on the sidewalls, whereas the other two components have their peak amplitude near the corners, outside the gap. This is an indication that the corner regions play a strong role in the guiding characteristics of this waveguide and that the effective index method is inadequate.

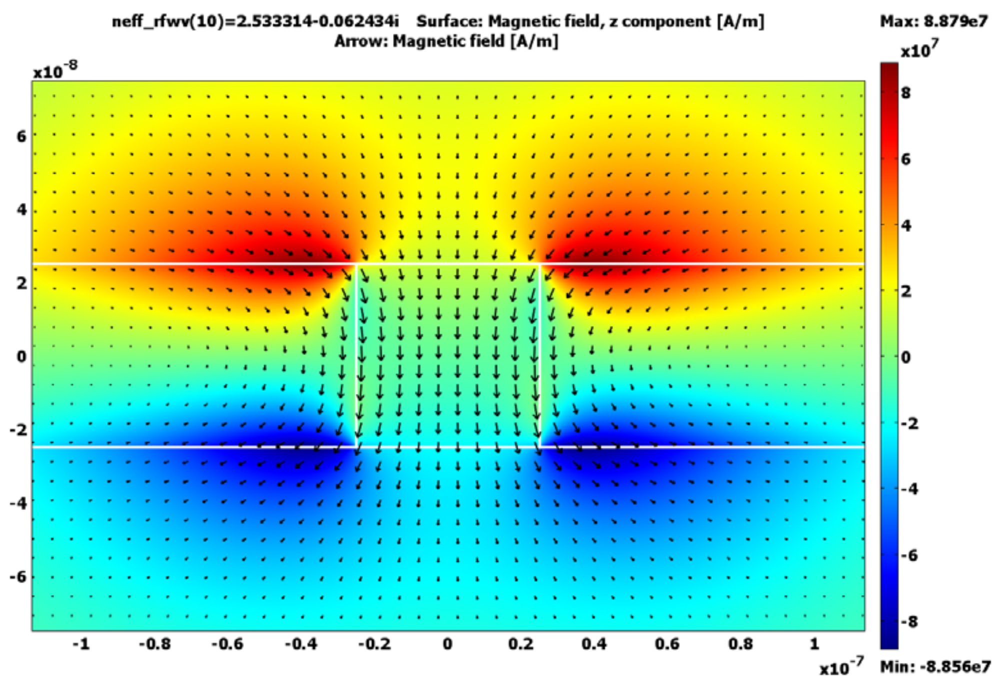

Figure 5.2a: Color plot of H_z and arrow plot of transverse *H* over the transverse plane for mode E^{x}_{11}, generated using the *COMSOL*™ commercial FEM package**.**

The electric field distribution of E^{x}_{11} shows how the fundamental mode resembles that of a capacitor, where the transverse electric field points almost straight across the gap. The *X* component of the electric field is strongly enhanced near the corners, indicating that a lot of displacement charge density is building up in a region where it is confined two-dimensionally. The electric field is more confined to the gap region than is the magnetic field. In fact, of all six field components, H_Z tends to be the least confined and therefore is good as a litmus test for deciding whether or not a mode is guided.

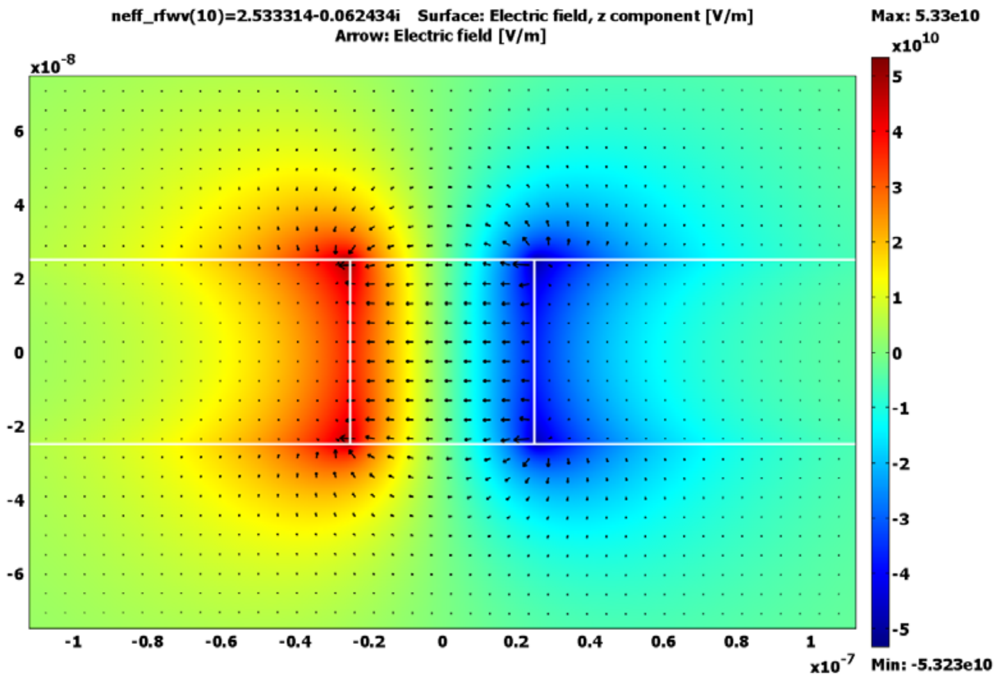

Figure 5.2b: Color plot of E_z and arrow plot of transverse E over the transverse plane for mode E_{11}^{x}, generated using the *COMSOL*™ commercial FEM package**.**

As has been discussed previously, the power flow transverse to the direction of propagation is into the metal, and Figure 5.3c corroborates this. The greatest rate of power flow is horizontally along the center of the gap in the *X* direction. The power flow in the *Z* direction is primarily at the four corners of the core, though a significant amount also occurs along the vertical sidewalls. There is, as expected, negative power flow inside the metal and this is also largest near the four corners.

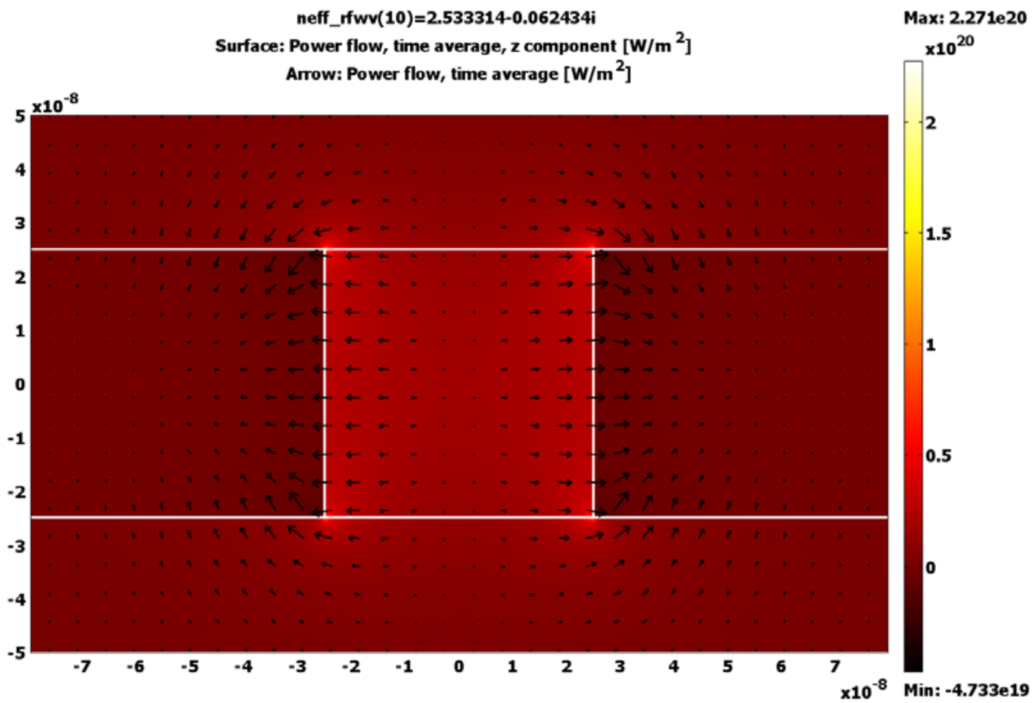

Figure 5.2c: Color plot of the *Z* component of the time average power flow and arrow plot of transverse time average power flow over the transverse plane for mode E^x_{11}, generated using the *COMSOL*™ commercial FEM package**.**

The magnetic and electric field distributions, along with the time average power flow are plotted in Figures 5.3a, 5.3b, and 5.3c for modes E^x_{21}. All of the fields are of this mode are less confined than the fundamental mode, especially the *Z* components. As expected, H_y and E_x have a field intensity minimum along a vertical line in the middle of the gap. The field components still show strong enhancement near the corners, demonstrating that a *single metal edge itself could be used to confine light*, and that the spacing between the metal corners of this waveguide must have a significant effect on the wave's confinement.

Given that the field components are less confined for this mode, the power flow in the *Z* direction is subsequently less confined as well. The transverse power flow for this mode looks very much like that of the fundamental mode, except that it is vertically asymmetric. Some type of asymmetric is expected since the refractive index of the cover and core are higher than that of the substrate. The power flow into the metal is larger where the refractive index is higher, a caveat showing that increasing the confinement of the light by increasing the index of the dielectric will also lead to more loss.

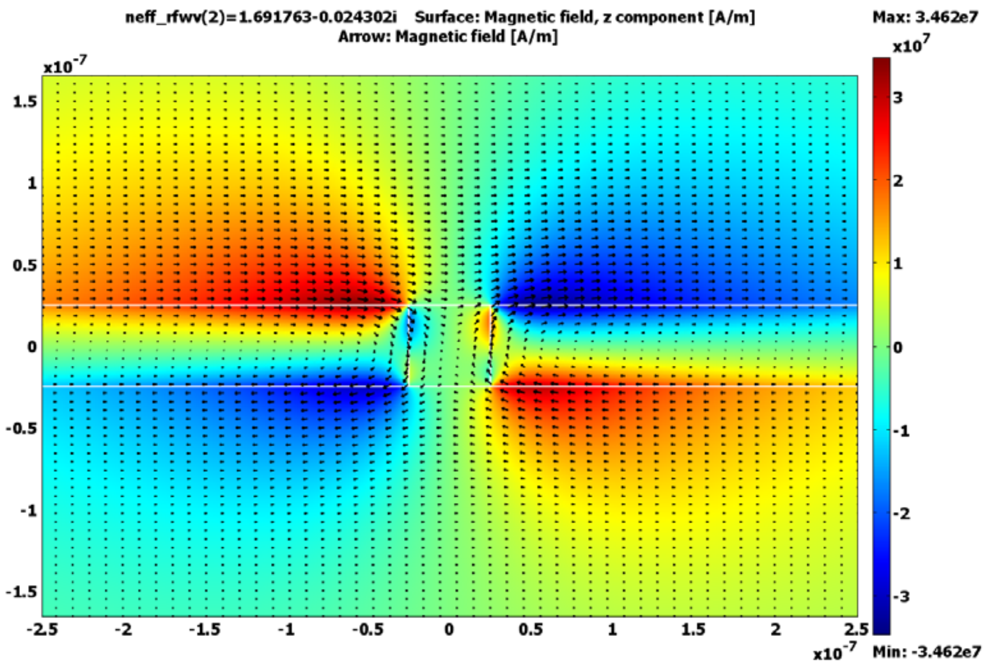

Figure 5.3a: Color plot of H_z and arrow plot of transverse H over the transverse plane for mode E^x_{21}, generated using the *COMSOL*™ commercial FEM package**.**

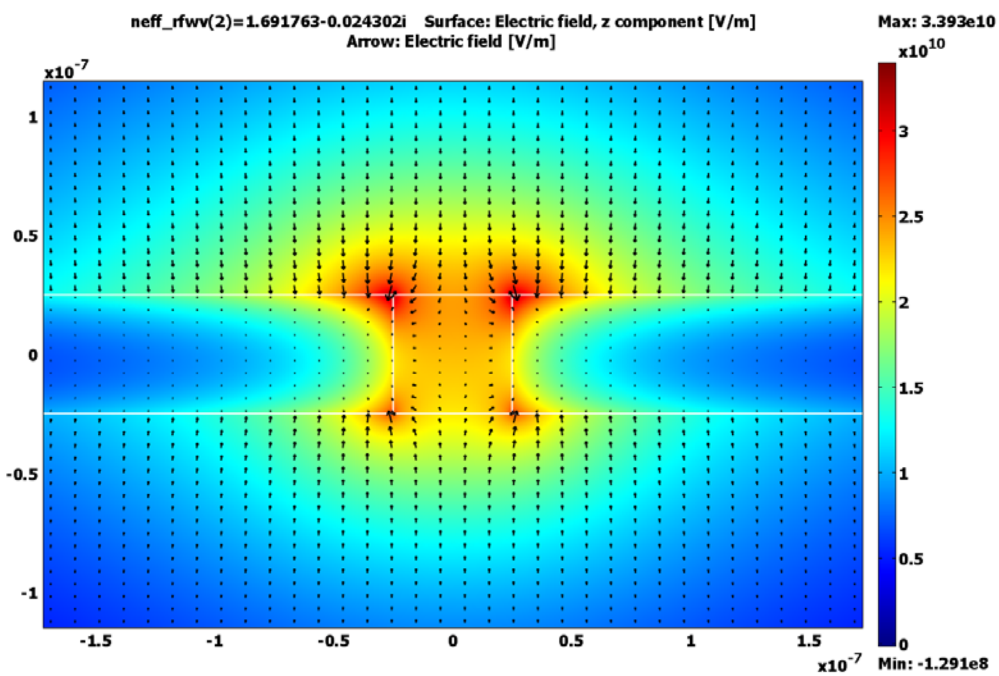

Figure 5.3b: Color plot of E_z and arrow plot of transverse E over the transverse plane for mode E^x_{21}, generated using the *COMSOL*™ commercial FEM package**.**

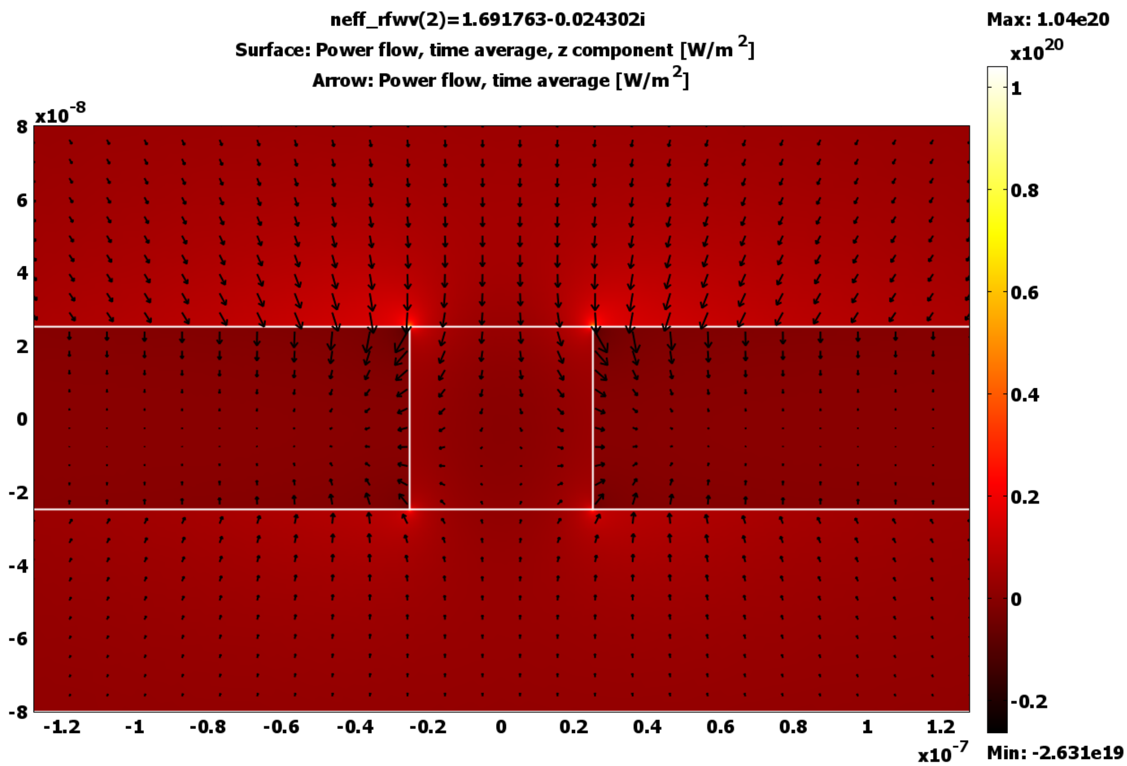

Figure 5.3c: Color plot of the *Z* component of the time average power flow and arrow plot of transverse time average power flow over the transverse plane for mode E^x_{21}, generated using the *COMSOL*™ commercial FEM package**.**

The gap is able to support more modes if it is made taller. Below in Figure 5.4 is shown the H_y profiles of the five modes that this structure is able to support when the height is increased to 500 nm. As someone familiar with waveguiding would anticipate, the taller gap supports modes that have more transverse oscillations vertically, which here are E^x_{12} and E^x_{13}. Because of the large aspect ratio of the gap, the E^x_{21} mode has split into two modes, one guided on the top, and one guided on the bottom. This interesting feature shows that a slight index asymmetry (again, the cover and core have an index of 1.49, and the substrate's index is 1.47) between the cover and substrate regions can lead to a shift of the power towards the side of the waveguide with the higher index, an attribute that could be used to build some kind of switch.

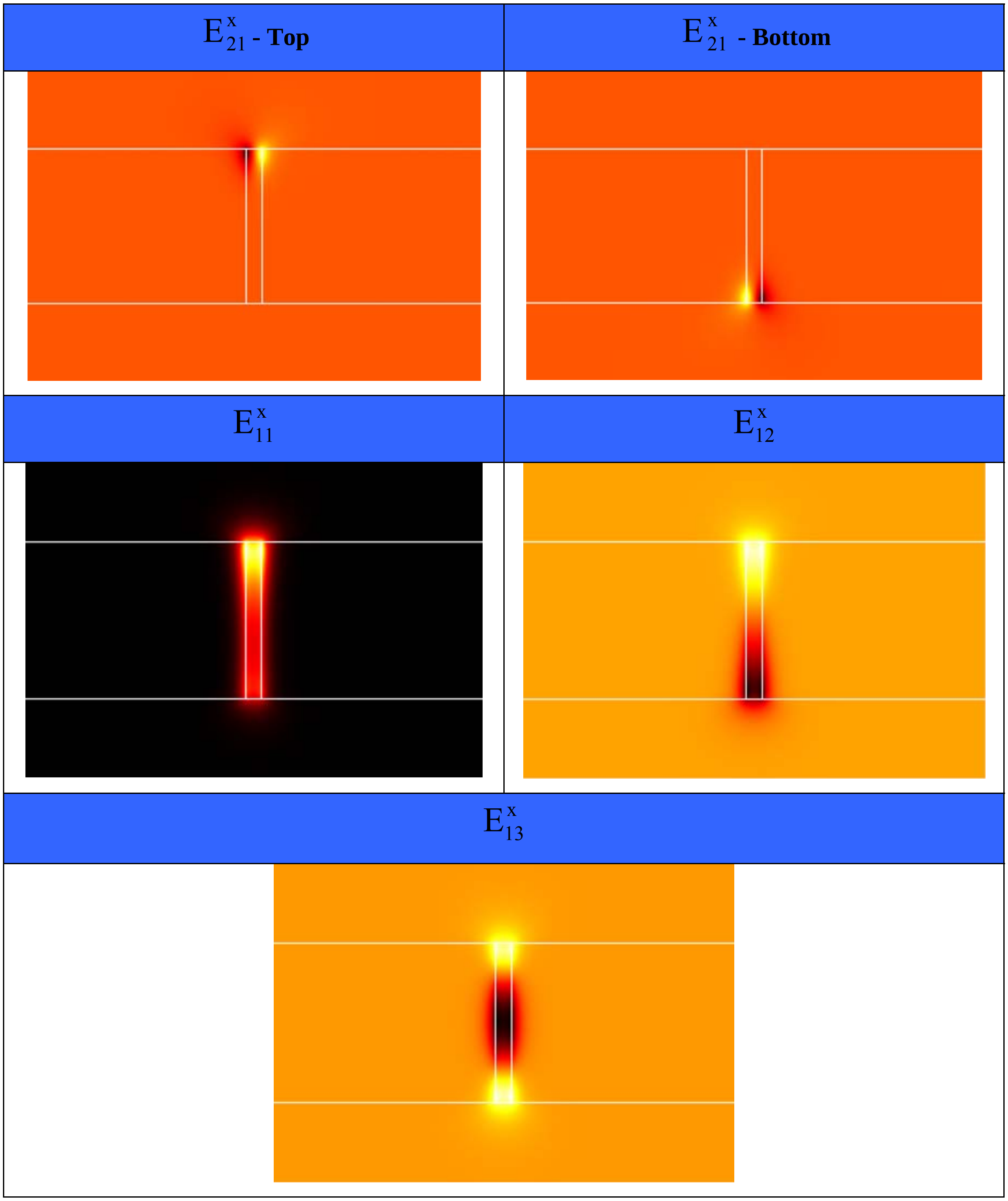

Figure 5.4: H_y (real component) mode profiles of the plasmon gap studied by Han, He and Liu for the case of a 500 nm tall gap. The white lines show the boundaries between the different regions of the gap waveguide, generated using the *COMSOL*™ commercial FEM package**.**

5.2: Propagation Characteristics of the Modes Supported by the Gap

Having seen the mode patterns, it is important to examine how their propagation characteristics change as a function of waveguide parameters. Since the free space wavelength, gap width, and core refractive index were already explored in Chapters 3 and 4, the focus of this chapter will be on sweeping the gap height. The height was swept as a parameter from 25 nm to 500 nm. Figure 5.5 below shows the results of the study. The first thing to note is that the propagation constants obtained using FEM and FDTD do not closely match up with the HHL ones at all. The fact that FEM and FDTD give the similar results for E_{11}^{x} suggests that the FEM used here is producing viable results for the real part of n_{eff}. It does make sense, from looking at the field distributions, that decreasing the gap height should actually *increase* the confinement of the mode (roughly measured by Re(n_{eff})) because the field is guided and confined by the four metal corners of the gap. Bringing the corners closer together here is analogous to making the width of the slab narrower for the two-dimensional case discussed in the last chapter. Though these results go against those reported by HHL in [43], they are corroborated by the work done by Pile, et al in [48]. The way that the effective index of E_{12}^{x} and E_{13}^{x} determined by FEM roughly match up with E_{11}^{x} and E_{12}^{x} determined by HHL using FD suggests that they may have incorrectly assigned effective indices to mode profiles.

All of the E_{1q}^{x} modes seem to approach the asymptote of the effective index for the infinitely tall gap (i.e. light guided between the two corners along the top of the gap, green line) rather than the effective index of the ideal metal-insulator-metal (MIM) slab with the same core index (cyan line). HHL were correct in their assertion that the effective index for the insulator-metal-insulator slab (infinitely wide Ag film between refractive indices of 1.47 and 1.49) acts as the cutoff for the modes propagating in the gap, because E_{11}^{x}, E_{12}^{x}, and E_{13}^{x} are cutoff at some point and do not show up. Mode E_{21}^{x} has an effective index a small amount above this cutoff level. For gap heights somewhere above 100 nm, this mode splits into two decoupled modes, one propagating along the top of the waveguide, and another propagating along the bottom, with the one on the bottom being less confined due to the slightly smaller refractive index. Though the bottom E_{21}^{x} mode appears to have a propagation constant less than that of the metal film (bounded on the top by n = 1.49, and on the bottom by n = 1.47given by the yellow stars), when one inspects its field components, one can see that it remains a guided mode.

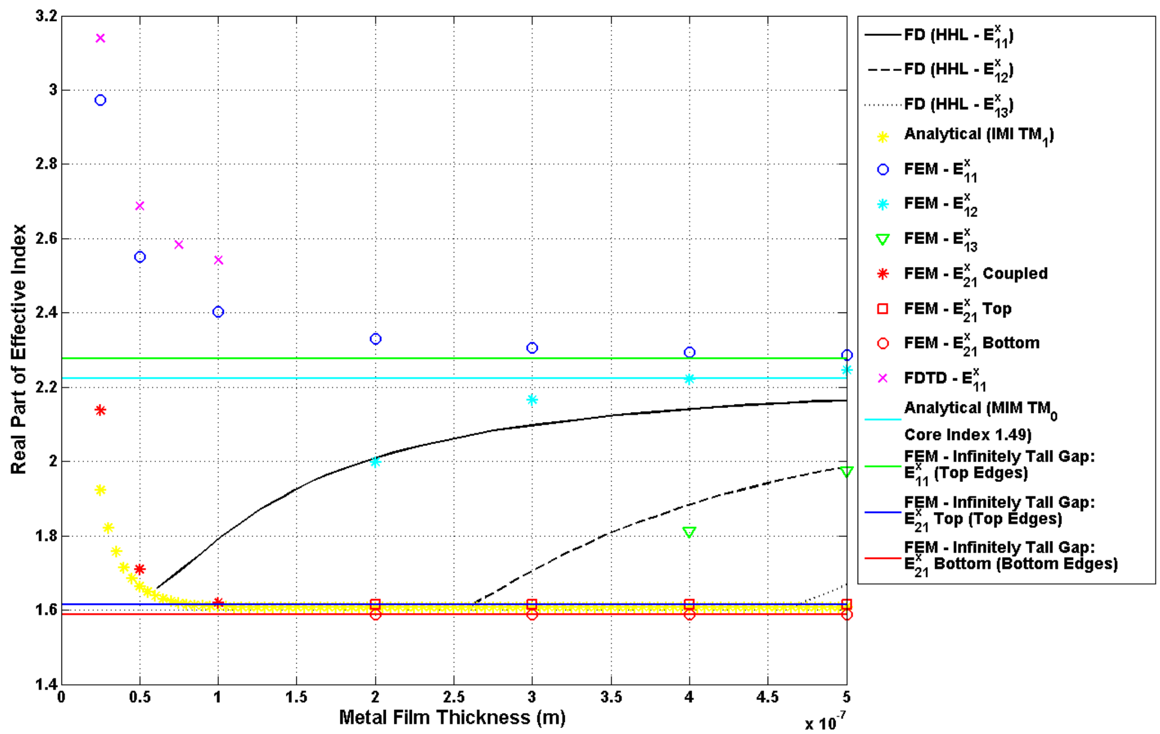

Figure 5.5: This shows the real parts of the effective indices as a function of gap height for the modes of the plasmon gap studied by Han, He, and Liu using different numerical methods, and comparing these to those obtained using analytical methods for asymptotic comparison.

Figure 5.6 below gives the power propagation lengths (as defined in Equation 4.2.9) for the modes of Figure 5.5. Here E^x_{21} shows the remarkable attribute of having a propagation length about four times that of the fundamental mode. When this mode splits into the top and bottom modes, the bottom mode has a longer propagation length. This is consistent with the observation that this mode, being mostly outside of the gap, is less confined that the fundamental mode. The E^x_{21} propagation lengths asymptotically converge on the one obtained for the corresponding E^x_{2q} mode propagating in an infinitely high gap. Using this mode is tempting because of its long propagation length; however, its localization near the corners and its low degree of confinement would make it difficult to excite experimentally, and so this mode is really of no practical use at the moment. The E^x_{1q} modes have propagation lengths about one quarter of the previously discussed ones, and these converge asymptotically to the E^x_{1q} mode propagating in the infinitely high gap as well. As with the two-dimensional slab waveguide, E^x_{13} ends up having the larger propagation length of all the higher order modes. The propagation length for E^x_{11} determined using FEM matches up reasonably well with that determined by HHL. Unfortunately, the propagation lengths determined using FDT D for E^x_{11} jump around quite a bit, indicating that either the grid or the time step was not sufficient to obtain converged results. The thing making FDTD difficult for plasmonic waveguides is the high grid density required to resolve features of the waveguide, which leads to a large increase in the simulation time required due to the stability condition putting a maximum limit on the time step (often referred to as the Courant condition) [49].

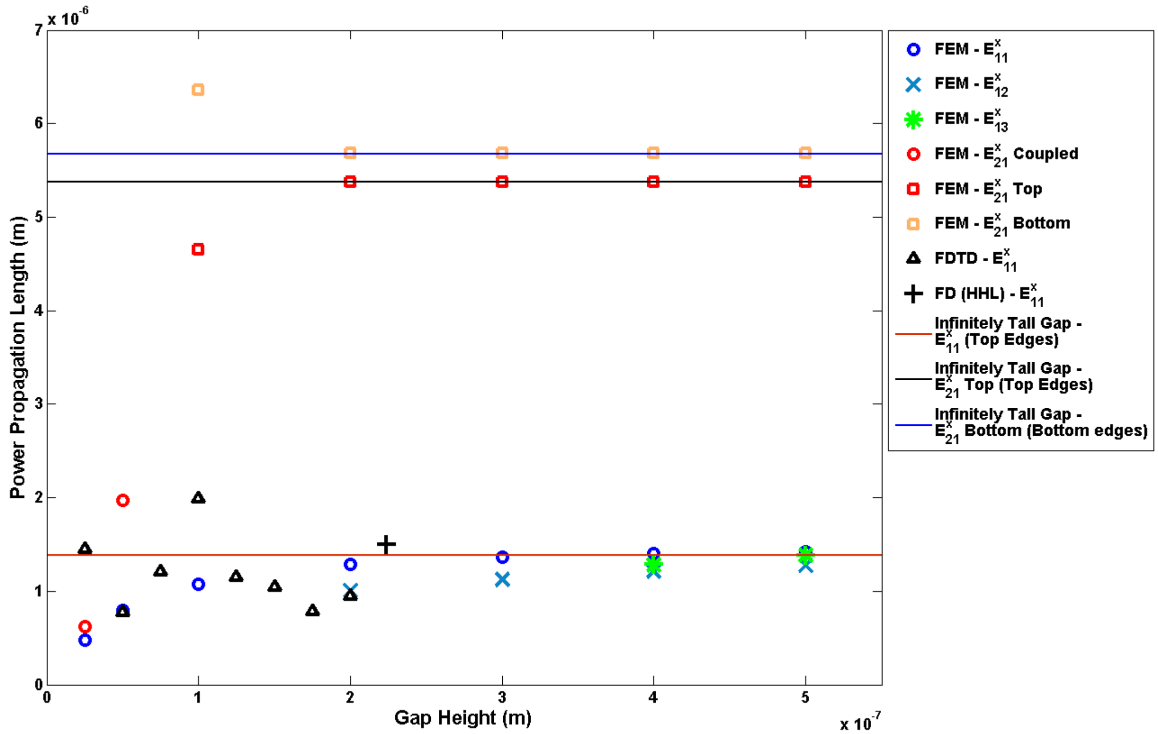

Figure 5.6: Power propagation lengths for the modes of the plasmon gap studied by Han, He, and Liu: comparison of HHL, FEM, and FDTD data.

5.3: FEM Convergence Study

To more efficiently use computational resources for FEM analysis, one would like to know how coarse he can make the mesh and how small the simulation domain to remain converged to within a certain percentage of the limiting value of his solution. Convergence studies are done to determine this. The purpose of this study is to determine what simulation domain sizes (relative to the free space excitation wavelength) and maximum mesh element sizes along the vertical sidewalls of the gap result in "converged" propagation constants for mode E^x_{11}. The same waveguide studied above, with the HHL parameters, was used. The height of the gap was taken to be 25 nm. The simulation domain was a square of variable width. For the mesh size study, the simulation domain width was held at a constant value of three times the free space wavelength of 632.8 nm, and the mesh element size was varied from 0.01 nm to 10 nm. For the simulation domain study, the mesh size was fixed at 1 nm, and the simulation domain size was swept from one to ten times the free space wavelength. The EGR was fixed at 1.1 for all of these studies. Due to limited computational resources, a sensitivity analysis of the EGR was not done, though it is something that should be done in the future as it determines the spread of the fine elements near the region of interest.

Figure 5.7 below gives the results of the mesh size study for the real part of the propagation constant. As the maximum element size is made smaller, the real part of the effective increases to a limiting value of about 2.976. The message here is clear: using a maximum element size of 1 nm will allow the propagation index to converge to within 0.1 % of its limiting value. The corresponding analysis for the imaginary part of n_{eff} leads to the same conclusion.

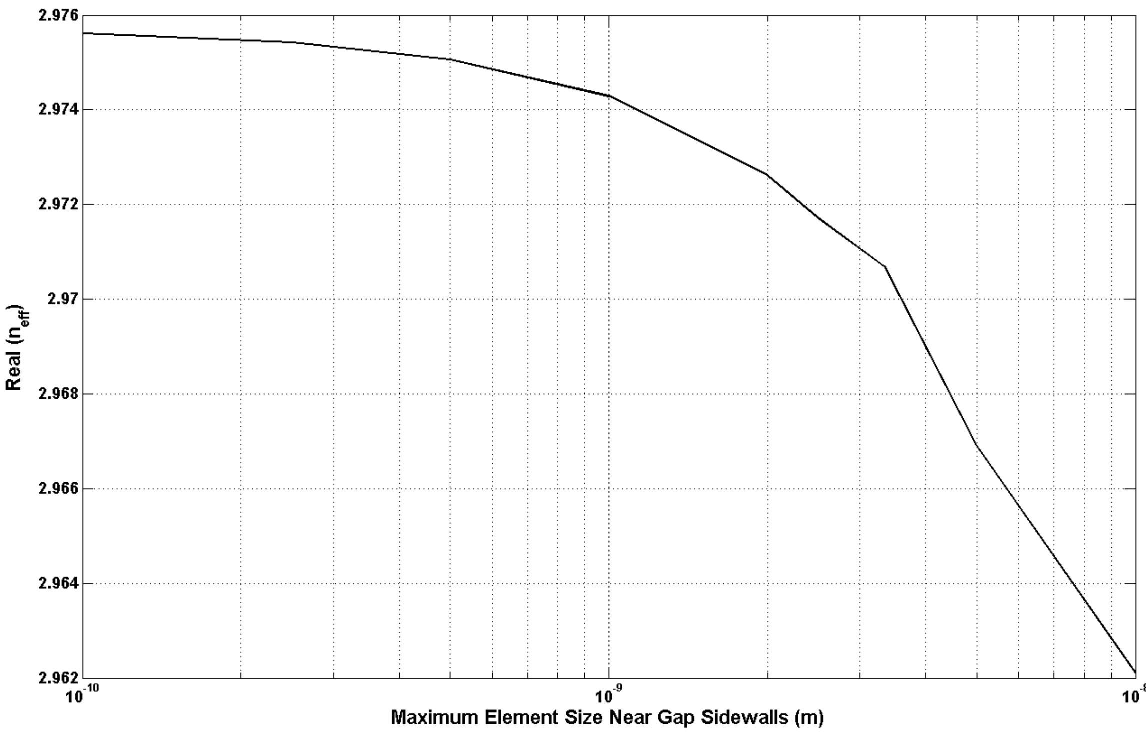

Figure 5.7: Real part of the effective propagation index in a 25 nm tall HHL plasmon gap versus maximum FEM element size near the gap sidewalls.

Figure 5.8 below shows the results for the simulation domain size study. It shows that only simulation domain size three times that of the free space wavelength is necessary to converge to well within one percent of the final limiting value. Again, the corresponding study of the imaginary part of the propagation constant yields the same conclusion.

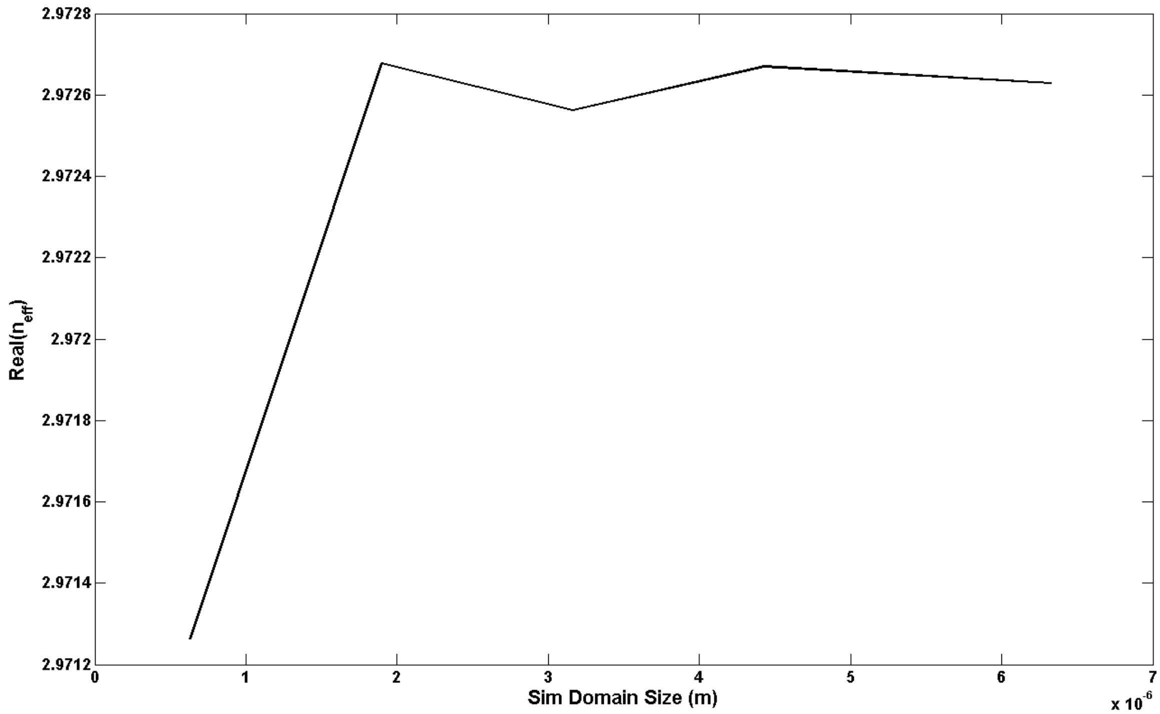

Figure 5.8: Real part of the effective propagation index in a 25 nm tall HHL plasmon gap versus the width of the simulation domain.

Thus, in order to obtain converged results with this particular waveguide and mode, with an EGR of 1.1, one merely needs to set the mesh size to 1 nm and keep the simulation domain width equal to three times the free space wavelength. This is not generalizable even to higher modes of this structure because the higher order modes are less confined and may be numerically truncated to a higher degree by a given simulation domain and mesh.

5.4: Key Points

In this chapter, the power and field profiles, propagation characteristics, and convergence stipulations for the finite height plasmonic gap were obtained for the Han-He-Liu waveguide parameters. For all modes examined, it was found that the power of the wave was localized near the corners of the core, indicating that the corners play a large role in the confinement of the wave, along with the metallic sidewalls. The time average power flow in the propagation and transverse directions is consistent with what was seen during the analytical analysis of the ideal two-dimensional slab: the power flows into the metal as the wave propagates, and the power propagating in the metal is in the direction opposite to the propagation direction. For gaps only 50 nm high, using waveguide parameters from Han-He-Liu, two guided modes are observed. For gaps 500 nm high, two more modes, with higher order field oscillations vertically, appear, and the

E^x_{21} mode is seen to split into two modes, one guided along the top two corners of the waveguide, and the other guided along the bottom two. This is due to the asymmetric refractive index distribution used. The modes E^x_{11} and E^x_{21} become more confined (larger Re(n_{eff})) as the gap height is decreased, whereas the higher order modes (E^x_{12} and E^x_{13}) are cutoff when their propagation constant approaches that of the symmetric mode of the polymer-Ag-polymer film slab. All of the modes have a decreasing power propagation length with decreasing gap height, but the E^x_{21} shows a much larger propagation length than the other modes, by about a factor of four for slab heights greater than 200 nm. The fundamental mode has the largest propagation length of all of the E^x_{1q} modes. All of the modes displayed power propagation lengths less than 6 μm, and so this particular waveguide is probably not much use as interconnect. One could decrease this loss by making the core larger (to say 100 nm), decreasing the core index, and/or increasing the free space wavelength. The convergence study of the FEM used showed that, when using an EGR of 1.1, and a gap height of 25 nm, that converged propagation constants can be obtained, to less than 0.1 % accuracy, by setting the simulation domain size to three times the free space wavelength (here 632.8 nm) and the maximum element size near the sidewalls to be 1 nm.

Conclusions

Computing devices have become an integral part of society's functioning and will continue to increase in importance as they become more compact and powerful. Currently, microprocessors rely on signal propagation by means of the charging and discharging of metal wires. This process is fundamentally limited by the resistance-capacitance (RC) time delay constant of the metal wire, which increases as the wires are made smaller in order to connect smaller transistors. This is making it increasingly difficult to shrink the size of transistors in order to realize faster switching and more transistors per unit area without actually slowing the circuits down. This is a motivation for the development of a new type of interconnect, using light as the signaling mechanism instead of electric charges. Light has the advantage of being able to propagate at a speed about three orders of magnitude greater than that of the saturation velocity of an electron along a wire. The price that one pays is that photons are inherently less confined than electrons when they propagate in dielectric waveguides. One technique for defeating this diffraction limit is to fabricate waveguides from materials whose real component of their relative electric permittivity is negative. Usually, noble metals are used as this material due to their low loss at optical frequencies. If the magnitude of this permittivity is greater than that of the surrounding dielectric, a surface plasmon wave is supported. This wave consists of a longitudinally compressive charge density oscillation along the interface between the dielectric and the metal. This wave, because it can have the same frequency as electromagnetic radiation in the infrared and visible spectra manifests itself as a light wave localized to the surface.

This localization has been used to defeat the diffraction limit of light by using various types of waveguiding structures. Structures that consist of dielectric gaps sandwiched between two metal layers show the best tradeoff between loss and confinement compared to other structures and also are isolated horizontally from other waveguides, allowing for degrees of integration. Physically realizable analogs of this consist of gaps etched into metallic films. Usually, metals such as Ag, Au, and Al are used, along with dielectrics such as polymethymethacrylate (PMMA), air, or silica. Gap sizes are 50 – 100 nm wide and tall. The light propagating in such waveguides has a finite propagation length because of absorption of the wave's energy due to ohmic-type losses as the electrons oscillate in the metal. This can be seen by looking at the time average power flow (Poynting vector) in the direction transverse to that of propagation, where the power of the wave flows into the metal. The power flow in the direction of propagation is localized at the four corners of the gap, and along the gap's vertical sidewalls. Different modes are supported depending on the height to width aspect ratio of the gap. The fundamental mode is of primary interest due to the ease of exciting it and its low loss. This mode is also known as the "capacitor mode" because the transverse electric field points across the gap without changing direction as in a capacitor. This mode actually becomes more confined as the dimensions of the waveguide are made smaller, although the loss of this mode, as with all the others, increases rapidly with smaller dimensions. The loss also increases for wavelengths decreasing towards the plasmon resonance of the structure, and so using longer wavelengths can aid in decreasing the loss. Another way to decrease the loss is use lower refractive index materials, down to about $n = 1.5$ to maximize the propagation distance.

The goal of this project was to obtain a body of knowledge concerning waveguiding using plasmonic gap structures, with intended application for interconnect in optical integrated circuits. There is still much work to be done. The propagation distance needs to be increased much larger than the ~ 6 microns obtained in this investigation for practical circuits to be realized. Once the waveguide has been optimized, devices need to be fabricated that could utilize it. Ideally, these devices would be all-optical switches because electrically-driven switches are still limited by RC time constants. Since plasmonic gap waveguides can confine a lot of power to a small cross section, on the order of 100 nm square, materials with a nonlinear, intensity-dependent refractive index could be used in the cores of the waveguides, allowing for the control of one light pulse with another. Such materials used within the gap core could be used to construct a compact "optical transistor."

References

[1] Internet: http://www.intel.com/museum/archives/4004.htm. Accessed 5-3-07.

[2] Internet: http://www.intel.com/museum/archives/pcturns25.htm Accessed 5-3-07.

[3] Internet: ftp://download.intel.com/museum/Moores_Law/Articles-Press_Releases/Press_Release_Aug2004.pdf Accessed 5-3-07.

[4] Internet: http://www.intel.com/technology/silicon/45nm_technology.htm?iid=search Accessed 5-3-07.

[5] J. Davis, R. Venkatesan, A. Kaloyeros, M. Beylansky, S. Souri, K. Banerjee, K. Saraswat, A. Rahman, R. Reif, J. Meindl. "Interconnect Limits on Gigascale Integration (GSI) in the 21st Century" *Proceedings of the IEEE*, vol. 89, pp. 305 – 324, 2001

[6] J. Conway, S. Sahni, and T. Szkopek. "Plasmonic Interconnects versus Conventional Interconnects: A Comparison of Latency, Cross-Talk, and Energy Costs" *Optics Express* vol. 15, pp. 4474-4484, 2007.

[7] P. Tran. "All-Optical Switching with a Nonlinear Chiral Photonic Bandgap Structure" *Journal of the Optical Society of America B*, vol. 16, pp. 70 – 73, 1999.

[8] W. Biehlig, F. Lederer, and E. Weinert-Raczka. "Nonlinear Antiresonant Reflecting Optical Waveguide Coupler with an Optically Induced Grating" *Journal of the Optical Society of America B*, vol. 14, pp. 3232 – 3237, 1997.

[9] C. Madsen and J. Zhao. "Increasing the Free Spectral Range of Silica Waveguide Rings for Filter Applications" *Optics Letters*, vol. 23, pp. 186-188, 1998.

[10] A. Boltasseva et alii. "Nanoimprinted Long-Range Surface Plasmon Polariton Waveguide Components" *Quantum Electronics and Laser Science Conference*, paper QMI6, 2006.

[11] M. De Jesus, K. Giesfeldt, J. Oran, N. Abu-Hatab, N. Lavrik, and M. Sepaniak. "Nanofabrication of Densely Packed Metal-Polymer Arrays for Surface-Enhanced Raman Spectroscopy" *Applied Spectroscopy*, vol. 59, pp. 1501 – 1508, 2005.

[12] M. Christiansen, M. Schøler, and A. Kristensen. "Integration of Active and Passive Polymer Optics" *Optics Express*, vol. 15, pp. 3931-3939, 2007.

[13] P. Bhattacharya. Semiconductor Optoelectronic Devices. Second Edition. © 2005 Prentice-Hall of India, New Dehli – 110 001. pg. 102.

[14] S. Maier, M. Brongersma, P. Kik, S. Meltzer, A. Requicha, H. Atwater. "Plasmonics – A Route to Nanoscale Optical Devices" *Advanced Materials*, vol. 13, 1501 – 1505, 2001.

[15] M. Kobrinsky, et al. "On-Chip Optical Interconnects" Internet: http://download.intel.com/technology/itj/2004/volume08issue02/art05_on-chip/vol8_art05.pdf *Intel Technology Journal*. vol. 8, pp. 129 – 142, 2004. Accessed 5-3-07.

[16] U. Fano. "The Theory of Anomalous Diffraction Gratings and of Quasi-Stationary Waves on Metallic Surfaces (Sommerfeld's Waves)" *Journal of the American Optical Society A*, vol. 31, pp. 213-222, 1941.

[17] E. Economou. "Surface Plasmons in Thin Films" *Physical Review*, vol. 182, pp. 539-554, 1969,

[18] I. Kaminow, W. Mammel, and H. Weber. "Metal-Clad Waveguides: Analytical and Experimental Study" *Applied Optics*, vol. 13, pp. 396-405, 1974.

[19] W. Barnes, A. Dereux, and T. Ebbesen. "Surface Plasmon Subwavelength Optics" *Nature*, vol. 424, pp. 824-830, 2003.

[20] Stefan Maier, PhD. Thesis. "Guiding of Electromagnetic Energy in Subwavelength Periodic Metal Structures." California Institute of Technology, Pasadena, CA. Defended January 24, 2003.

[21] G. Veronis and S. Fan. "Guided Subwavelength Plasmonic Mode Supported by a Slot in a Thin Metal Film" *Optics Letters*, vol. 30, pp. 2288 – 2290, 2005.

[22] P. Berini, R. Charbonneau, N. Lahoud, and G. Mattiussi. "Characterization of Long-Range Surface Plasmon-Polariton Waveguides" *Journal of Applied Physics*, vol. 98, 43109, 2005.

[23] J. Dionne, L. Sweatlock, H. Atwater, A. Polman. "Plasmon Slot Waveguides: Towards Chip-Scale Propagation with Subwavelength-Scale Localization" *Physical Review B*, vol. 73, 35407, 2006.

[24] P. Johnson and R. Christy. "Optical Constants of the Noble Metals" *Physical Review B*, vol. 6, pp. 4370 – 4379, 1972.

[25] S. Song et. al. "Vertical Coupling of Long-Range Surface Plasmon Polaritons" *Applied Physics Letters*, vol. 88, 11110, 2006.

[26] T. Fujisawa and M. Koshiba. "All-Optical Logic Gates Based on Nonlinear Slot-Waveguide Couplers" *Journal of the American Optical Society B*, vol. 23, pp 684 – 691, 2006.
[27] Lüth, Hans. <u>Solid Surfaces, Interfaces, and Thin Films</u>. Fourth Edition. Springer-Verlag. Berlin-Heidelberg-New York. © 2001. pg. 248.

[28] Ward, Leslie. <u>The Optical Constants of Bulk Materials and Films</u>. Institute of Physics Pub., Bristol, Philadelphia. © 2001. pp. 17-20.

[29] P. Nordlander and C. Oubre. "Optical Properties of Metallodielectric Nanostructures Calculated Using the Finite Difference Time Domain Method" *Journal of Physical Chemistry B*, vol. 108, pp. 17740 – 17747, 2004.

[30] Palik, Edward, editor. <u>Handbook of Optical Constants of Solids</u>. Academic Press, Orlando. © 1985. pp. 280-295, 333-341, 350-357 (for Cu/Au, Pt, Ag, respectively)

[31] Ulaby, Fawwaz T. <u>Fundamentals of Applied Electromagnetics (2004 Media Edition)</u>. Pearson Prentice Hall, Upper Saddle River, NJ 07458. © 2004. pp. 312-314.

[32] Boardman, A. D. Electromagnetic Surface Modes. John Wiley and Sons Ltd © August 18, 1982. p. 154.

[33] J. Burke, G. Stegeman, and T. Tamir. "Surface-Polariton-Like Waves Guided by Thin, Lossy Metal Films" *Physical Review B*, vol. 33, pp. 5186 – 5201, 1986.

[34] I. H. Malitson. "Interspecimen Comparison of the Refractive Index of Fused Silica," *Journal of the Optical Society of America,* vol. 55, pp. 1205 – 1209, 1965.

[35] M. Futamata. "Application of Attenuated Total Reflection Surface-Plasmon-Polariton Raman Spectroscopy to Gold and Copper" *Applied Optics*, vol. 36, pp. 364 – 375, 1997.

[36] R. Zia, et. al. "Geometries and Materials for Subwavelength Surface Plasmon Modes" *Journal of the Optical Society of America A*, vol. 21, pp. 2442 – 2446, 2004.

[37] J. C. Lagarias, J. A. Reeds, M. H. Wright, and P. E. Wright, "Convergence Properties of the Nelder-Mead Simplex Method in Low Dimensions," *SIAM Journal of Optimization*, vol. 9, pp. 112-147, 1998.

[38] Okamoto, Katsunari. Fundamentals of Optical Waveguides, Second Edition. © Academic Press, 2006. pg. 26.

[39] Okamoto, Katsunari. Fundamentals of Optical Waveguides, Second Edition. © Academic Press, 2006. pg. 19.

[40] S. Bozhevolnyi. "Effective-Index Modeling of Channel Plasmon Polaritons" *Optics Express*, vol. 14, pp. 9467 – 9476, 2006.

[41] This class was taken at The Ohio State University Autumn Quarter 2006, and was taught by Professor Ronald M. Reano. Email: reano@ece.osu.edu

[42] Okamoto, Katsunari. Fundamentals of Optical Waveguides, Second Edition. © Academic Press, 2006. pp. 37 - 40.

[43] Z. Han, S. He, and L. Liu. "Novel Surface Plasmon Waveguide for High Integration" *Optics Express*, vol. 13, pp. 6645 – 6650, 2005.

[44] M. Sadiku. Numerical Techniques in Electromagnetics. CRC Press, Boca Raton. © 2001. Chapter 9.

[45] P. Berini. "Modeling Lossy Anisotropic Dielectric Waveguides with the Method of Lines" *IEEE Transactions on Microwave Theory and Techniques*, vol. 44, pp. 749 – 759, 1996.

[46] P. Berini. "Plasmon-Polariton Modes Guided by a Metal Film of Finite Width Bounded by Different Dielectrics" *Optics Express*, vol. 7, pp. 329 – 335, 2000.

[47] Okamoto, Katsunari. Fundamentals of Optical Waveguides, Second Edition. © Academic Press, 2006. pg. 29.

[48] Pile, et alii. "Two-Dimensionally Localized Modes of a Nanoscale Gap Plasmon Waveguide" *Applied Physics Letters*, vol. 87, 261114, 2005.

[49] K. Yee. "Numerical Solution of Initial Boundary Value Problems Involving Maxwell's Equation in Isotropic Media" *IEEE Transactions on Antennas and Propagation*, vol. 14, pp. 302 – 307, 1966.